RNA and RNA-protein complexes Principles of ion binding to RNA inferred from the analysis of a 1.55 Å resolution bacterial ribosome structure - Part I: Mg2+

Filip Leonarski, Anja Henning-Knechtel, Serdal Kirmizialtin, Eric Ennifar, Pascal Auffinger

Nucleic Acids Research, 2024, 1–21
https://doi.org/10.1093/nar/gkae1148
RNA and RNA-protein complexes

Principles of ion binding to RNA inferred from the analysis of a 1.55 Å resolution bacterial ribosome structure – Part I: Mg^{2+}

Filip Leonarski[1], Anja Henning-Knechtel[2], Serdal Kirmizialtin[2,3], Eric Ennifar[4] and Pascal Auffinger[4,*]

[1]Swiss Light Source, Paul Scherrer Institut, Villigen PSI 5232, Switzerland
[2]Chemistry Program, Science Division, New York University Abu Dhabi, Abu Dhabi, United Arab Emirates
[3]Department of Chemistry, New York University, USA
[4]Université de Strasbourg, Architecture et Réactivité de l'ARN, Institut de Biologie Moléculaire et Cellulaire du CNRS, 2 Allée Konrad Roentgen, 67084 Strasbourg, France
[*]To whom correspondence should be addressed. Tel: +33 3 88 41 70 00; Fax: +33 3 88 60 22 18; Email: p.auffinger@ibmc-cnrs.unistra.fr

Abstract

The importance of Mg^{2+} ions for RNA structure and function cannot be overstated. Several attempts were made to establish a comprehensive Mg^{2+} binding motif classification. However, such descriptions were hampered by poorly modelled ion binding sites as observed in a recent cryo-EM 1.55 Å *Escherichia coli* ribosome structure where incomplete ion assignments blurred our understanding of their binding patterns. We revisited this model to establish general binding principles applicable to any RNA of sufficient resolution. These principles rely on the 2.9 Å distance separating two water molecules bound in *cis* to Mg^{2+}. By applying these rules, we could assign all Mg^{2+} ions bound with 2–4 non-water oxygens. We also uncovered unanticipated motifs where up to five adjacent nucleotides wrap around a single ion. The formation of such motifs involves a hierarchical Mg^{2+} ion dehydration process that plays a significant role in ribosome biogenesis and in the folding of large RNAs. Besides, we established a classification of the Mg^{2+}…Mg^{2+} and Mg^{2+}…K^{+} ion pairs detected in this ribosome. Overall, the uncovered binding principles enhance our understanding of the roles of ions in RNA structure and will help refining the solvation shell of other RNA systems.

Graphical abstract

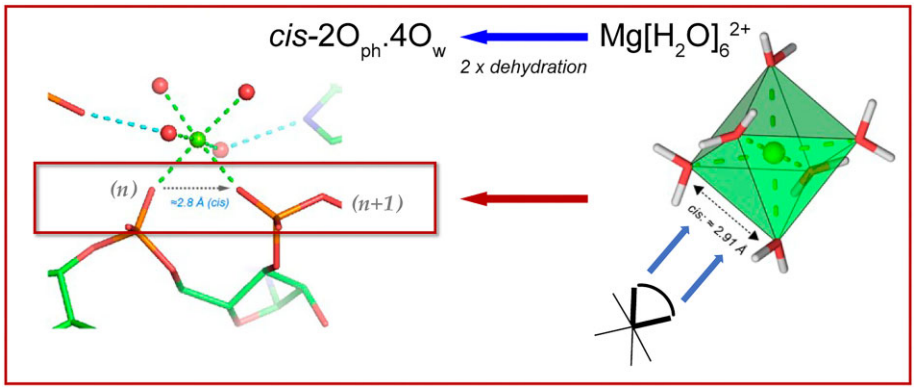

Introduction

Since the earliest biochemical studies on ribosomes, Mg^{2+} along with K^{+} and polyamines were found to be essential for the structure and function of these systems (1–8). The first ribosome structure that allowed the assignment of mono- and divalent ions was that of the 50S *Haloarcula marismortui* large subunit (*Hm*-LSU) by Steitz and co-workers (9). A comprehensive study on the identification of Mg^{2+}, Na^{+} and K^{+} ions based on this structure was subsequently published by these authors (10). To date, several hundreds of ribosomal cryo-EM/X-ray structures have been deposited to the Protein Data Bank (PDB) with resolutions ranging from 1.55 to over 4.0 Å (11). The number of assigned Mg^{2+} ions varies from zero for the most cautious authors to ≈1260 Mg^{2+} per 70S ribosome (or one Mg^{2+} per three nucleotides) as in a 2.3 Å resolution *Thermus thermophilus* structure (12) or close to full neutrality as in another 3.1 Å resolution *T. thermophilus* (13) structure (PDBid: 4V6F; ≈2 970 Mg^{2+}/70S). These numbers are in stark contrast, with the 138 Mg^{2+}, 85 Na^{+}, 2 K^{+}, 5 Cd^{2+} cations and the 30 Cl^{-} and 4 acetate anions assigned

Received: April 9, 2024. **Revised:** July 22, 2024. **Editorial Decision:** September 8, 2024. **Accepted:** November 1, 2024

in the latest 2013 refinement (14) of the (*Hm*-LSU) structure (PDBid: 4V9F; resolution: 2.4 Å).

Current estimates suggest that 100–300 site-bound Mg^{2+} ions per ribosome are reasonable depending on the system size and experimental conditions (3,7). Larger Mg^{2+} numbers may result from specific buffers or from an excess of confidence in the amount of information that can be extracted from experimental data. For RNA and other metal containing biomolecular systems, the latter bias has been documented (15–24). Some tools to identify assignment issues have been developed (25–29) but none specific to nucleic acids besides the critically evaluated MgRNA attempt (15,16,30).

To gain deeper insights into the biological functions of Mg^{2+} and K^+ ions, it is essential to advance our understanding of the binding stereochemistry of these ions. To this end, we re-examined the recent 1.55 Å resolution (PDBid: 8b0x) *Escherichia coli* 70S ribosomal cryo-EM structure that comprises 1 Zn^{2+}, 361 Mg^{2+}, 168 K^+ and 11 461 water molecules (11). However, a rapid examination of this structure revealed that ≈261 Mg^{2+} ions exhibit incomplete coordination shells and that about ≈28 K^+ with coordination distances around 2.8 Å were assigned as Mg^{2+} ions (Figure 1). Such inaccurate or incomplete assignments are a hurdle to database surveys (20,27,30) and limit the precision of artificial intelligence tools (31–35).

Here, we applied state-of-the-art stereochemical knowledge to establish criteria for validating the ionic structure of small RNAs up to large ribosomes. Correcting inaccurate ion assignments such as those described here and in previous reports is an essential prerequisite for the understanding of ion-binding features (15–17,19). This undertaking helps to lay the basis of a comprehensive Mg^{2+}/K^+ ion binding site classification and to improve ion positions in earlier and sometimes less well resolved structures. For instance, the authors of the 8b0x structure based part of their Mg^{2+}/K^+ assignments on those made in the 6qnr and 7k00 structures. This process led to some of the issues described herein (17,29,36,37).

By building on the previous MgRNA study (15,16,30) and seminal investigations by Steitz and Klein (10), we present an updated classification of Mg^{2+}-bindingsites and illustrate each of the identified ion-binding site categories. Using the amended 8b0x structure, we describe a set of simple stereochemical rules for positioning Mg^{2+} ions at key locations. We stress the importance of Mg^{2+} bidentate clamps and demonstrate that by scanning the OP…OP distances <3.4 Å, nearly 100% of these clamps can be accurately assigned. We infer that these Mg^{2+}-binding motifs are key to the processing of essential ribosome folding events occurring during biogenesis. We also discuss the formation of novel motifs, such as those involving Mg^{2+}…O2' coordination and propose a classification of Mg^{2+}…Mg^{2+} and Mg^{2+}…K^+ ion pairs which are frequently observed in both catalytic and non-catalytic systems.

Additionally, we describe rules to characterize the binding of 'chelated' hexahydrated $Mg(H_2O)_6{}^{2+}$ ions that are based on a correspondence between the local ribosomal RNA (rRNA) hydration structure and the Mg^{2+} hydration shell. This highlights the importance of thoroughly refining the solvation shell of RNA systems. However, diffuse $Mg(H_2O)_6{}^{2+}$ and K^+ ions, which dominantly contribute to the charge neutralization process, still escape direct observation even in high-resolution structures.

A few drawbacks associated with cryo-EM techniques can be noted. For instance, unlike X-ray experiments, cryo-EM does not provide differential maps despite some efforts made in that direction (38–40). Although anomalous signals can be obtained for identifying K^+ ions under very specific conditions (17,36,41,42), no current technique produces signals to directly identify Mg^{2+} ions. Therefore, in most instances, we have to rely on stereochemical criteria to assign Mg^{2+}/K^+ ions.

Despite these limitations, we believe that 8b0x is currently the best candidate for investigating the ribosomal ionic shell. Given the conservation of the ribosome core sequences and structures, we expect that a significant percentage of the chelated ions found in the *E. coli* ribosomes are conserved in archaea, bacterial and eukaryote systems (10,43–45). We anticipate that the use of the stereochemical rules established here will enhance our understanding of the solvation shell of nucleic acids and protein systems.

Due to space constraints, the binding features of K^+ ions (15,36,46–48) will be addressed in a companion paper.

Materials and methods

8b0x cryo-EM buffers

The final cryo-EM buffer contained 25 mM $Mg(OAc)_2$, 100 mM K(OAc), 50 mM HEPES and 1 mM DTT for a pH of 7.4 (11). Hence, it can be inferred that next to HEPES, DTT and possible contaminants (see below), only Mg^{2+} and K^+ cations along with acetate anions and water molecules are part of the 8b0x solvation shell. For *E. coli* ribosome structures with resolutions <2.0 Å, see **SI**.

Updated Cambridge Structural Database histograms for Mg and K

Distance and angle histograms for the Mg^{2+} and K^+ ions were derived from the Cambridge Structural Database (CSD version 5.43, update November 2022; see Figures 2 and 3) (49,50). These histograms are updated versions of those examined in previous studies (15,16,51). Only high-resolution structures were considered (R_factor ≤ 0.05 %). Disordered, error containing, polymeric and powder structures were discarded. All O/N atom types were considered with the exception of protonated nitrogens. Charge constraints were not applied given known arbitraryness in the CSD attribution process (52). Only hexacoordinated Mg ions were considered since their primary coordination number in biomolecules is 6. For potassium (K), no restrictions on the coordination number of coordinated atoms were applied as the coordination number can range from 6 to 9 (15,36,53). For additional potassium coordination features, see **SI**.

Mg coordination parameters

d(Mg…O/N) ≈2.07 ± 0.04 Å and d(Mg…N) ≈2.19 ± 0.08 Å are the average first shell distances for hexacoordinated Mg ions derived from the Figure 2 histograms. An exclusion zone specifying that no O/N atoms should be present in the 2.3–3.6 Å distance range was drawn for Mg. However, given stereochemical constraints associated with highly chelated Mg^{2+} motifs found in ribosomal structures but not in the CSD, we readjusted the upper exclusion zone limit from 3.6 to 3.4 Å (see **SI**). In the CSD histograms, d(Mg…N) distances longer by ≈0.10 Å over d(Mg…O) distances are observed. The origin of this offset remains unclear. It may in part be linked to the binding of bulky imidazole rings (54). Yet, the 2.19 Å co-

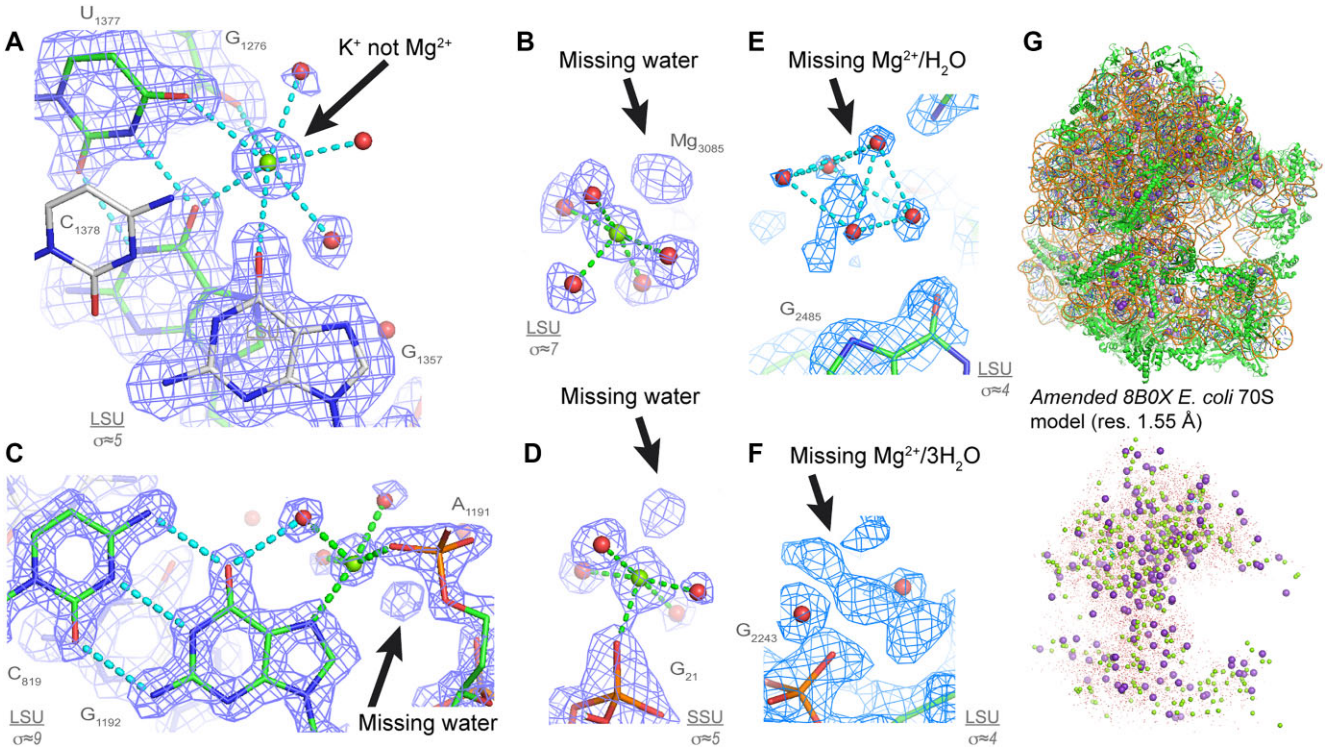

Figure 1. 8b0x ion assignments and first shell completion issues. **(A)** This Mg^{2+} ion has been assigned to the deep grove of a G•U pair (a neighbouring C = G pair has silver carbons). However, the heptahedral ion coordination with $d(Mg^{2+}…O) \approx 2.8$ Å implies that this ion is K^+ and not Mg^{2+}; see Figure 2 for distance criteria. **(B)** These $6O_w$, **(C)** $O_{ph}.N_b.4O_w$ and **(D)** $O_{ph}.5O_w$ ions display missing first shell waters. **(E)** A Mg^{2+} and a water belonging to a hexahydrated Mg^{2+} were not assigned. **(F)** The densities of this $O_{ph}.5O_w$ ion and of three waters were left empty. See Figure 4 for binding site nomenclature. Green/cyan lines mark distances <2.3 Å and in the 2.6–3.2 Å range. **(G)** View of the amended 8b0x model (top) and of its solvation shell (bottom) with 403 Mg^{2+} (green spheres), 231 K^+ (purple spheres) and 21 397 waters (red dots). Sigma levels are indicated where appropriate.

ordination distance is in line with the 2.17 Å distance derived from quantum mechanical calculations (55).

For Mg, the *cis-* and *trans-* coordination angles are $\theta(O…Mg…O) \approx 90 \pm 3°$ and $\theta(O…Mg…O) \approx 177 \pm 4°$. The resulting average distances between oxygen atoms in *cis-* and *trans-* are $d(O…O) \approx 2.93 \pm 0.09$ Å and $\approx 4.13 \pm 0.07$ Å, respectively (Figure 3).

Ion-binding site nomenclature

The ion-binding site nomenclature, extended to comprise amino acid atoms, is derived from the MgRNA study (15,16,30). O_{ph} corresponds to OP1/OP2 phosphate anionic oxygens, O_r to O2'/O4'/O3'/O5' ribose and phosphate bridging oxygens, O_b to nucleobase O2/O4/O6 oxygens and N_b to non-protonated nucleobase N1/N3/N7 nitrogens. Ion-binding sites are named by using a combination of these categories. For instance, $2O_{ph}.4O_w$ stands for a hexacoordinated ion bound to two O_{ph} atoms and four waters. The sites with two O_{ph} atoms in *cis-* or *trans-* and four water molecules are named *cis*-$2O_{ph}.4O_w$ and *trans*-$2O_{ph}.4O_w$. When three non-water atoms such as O_{ph} are attached to the ion, the corresponding isoforms become *fac*-$3O_{ph}.3O_w$ (*facial*) when the three O_{ph} pairs are in *cis-* and *mer*-$3O_{ph}.3O_w$ (*meridional*) when at least one O_{ph} pair is in *trans-* (30). When four non-water atoms are bound to the ion such as $4O_{ph}.2O_w$, the *cis-*/*trans-* terminology is used to name the respective orientation of the two bound water molecules. To distinguish them from the *cis-*/trans-$2O_{ph}.4O_w$ types, the *cis-*/*tr ans-* prefix (underlined with a capital) are used. Finally, this *cis-*/*trans-*/*fac-*/*mer-*/*c is-*/*t ran s-* nomenclature can be extended to any $O_{ph}/O_b/O_r/N_b$ atom combinations. For proteins, we used O_{bb} (previously O_{back}) for amino acid backbone oxygens, O_{coo} for Asp/Glu carboxyl oxygens, O_{cno} for Asn/Gln carbonyl oxygens, OH_{prot} for Ser/Thr/Tyr hydroxyl oxygens and N_{His} for non-protonated ND1/NE2 histidine nitrogens.

Ion identification issues and Phenix refinements

Mg^{2+}-binding sites are more difficult to identify when ions present one or more of the following flaws: (i) Mg^{2+} coordination distances that exceed the 2.3 Å limit, (ii) incomplete Mg^{2+} coordination shells, (iii) misassigned ions or (iv) unassigned ions (Figure 1). To identify these issues, we used the outputs of an in-house '*IonDiagnosis*' tool (17) previously developed (see **SI** for an 8b0x '*IonDiagnosis*' output). We 'idealized' the Mg^{2+} coordination shell through the addition of $d(Mg^{2+}…O/N) \approx 2.07/2.19$ Å distance restraints that allowed an improved ion-binding site assessment. Then, the modified 8b0x structure was refined in Phenix (56). We refrained using angle restraints that could have led to an inappropriate level of idealization (see next paragraph). This process resulted in an amended 8b0x model. The coordinates of this 1.0 model that comprises all the added/modified Mg^{2+}/K^+ ions and water molecules are available in the **SI**.

Consistency criteria used to check the assigned Mg^{2+} ion-binding sites

We used several criteria to estimate the consistency of the identified Mg^{2+}-binding sites. First, we checked the presence of six

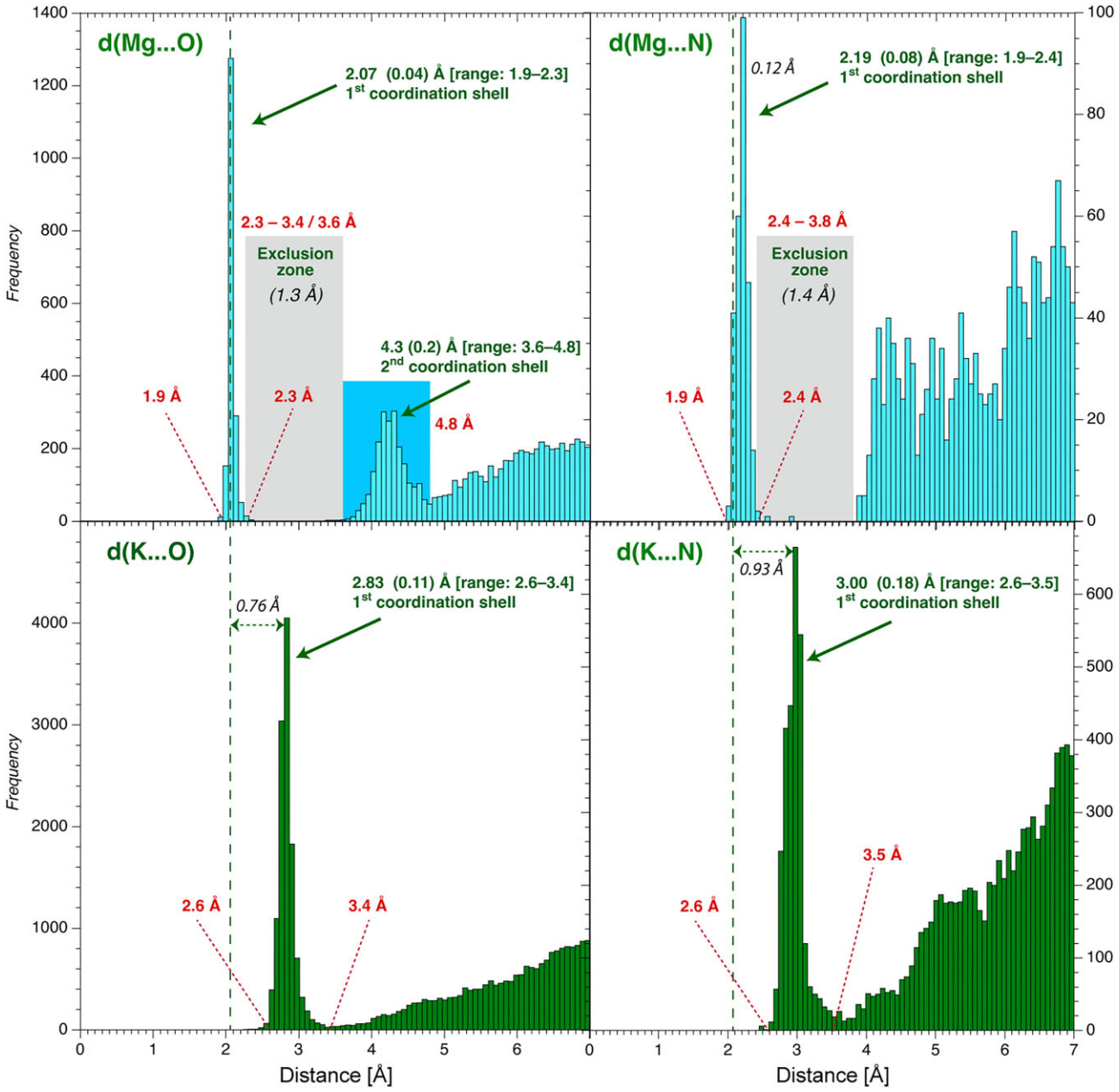

Figure 2. O/N coordination distance histograms for Mg/K derived from the CSD (version 5.43, update November 2022). (**Top**) See the Materials and method' section for CSD search criteria. Only hexacoordinated Mg ions were considered; no coordination number constraints were placed on K. First and second peak standard deviations are in parenthesis. All types of O and non-protonated N atoms were used to build these histograms (15,16,51). A vertical dashed line marks the average *d*(Mg…O) ≈2.07 Å coordination distance in all histograms. Mg exclusion zones are marked by grey rectangles. Note that we readjusted the 3.6 Å exclusion zone limit to 3.4 Å (see **SI**).

coordination distances in the 1.9–2.3 Å range. Then, the octahedral character of the coordination shell was assessed by calculating the angular deviations of the bound atoms. For that purpose, the hexacoordinated Mg^{2+} ions were classified into one of three categories: 'correct', 'slightly distorted' and 'highly distorted'. These categories are determined based on the deviation of the cumulated (ligand…Mg^{2+}…ligand) angular value associated with a regular coordination octahedron: $<5°$ for 'correct', in the 5–10° range for 'slightly distorted' and $>10°$ for 'highly distorted', respectively. The ions in the 'highly distorted' category are affected by local disorder, partial occupancy or any other factors that might blur their coordination patterns. As such, we refrained to include these 'distorted' ions in the 'well-defined' binding site counts of our survey unless otherwise specified. However, we included them in our amended 8b0x model.

A second consistency criterion was defined as follows. If the density peak of a given ion is below an arbitrary 4.0 Å r.m.s.d. value as defined by the Coot visualization program (57), this ion was excluded from our 'well-defined' Mg^{2+}-binding site ensemble. Further, if some coordinating atoms are found in the 2.3–3.4 Å exclusion zone, we tried to correct the stereochemistry of the binding site by imposing local restraints. If we were unable to find any rational for these 'exclusion zone' contacts, these ions were discarded. We note that the ions associated with 'not-well-defined' sites may have been appro-

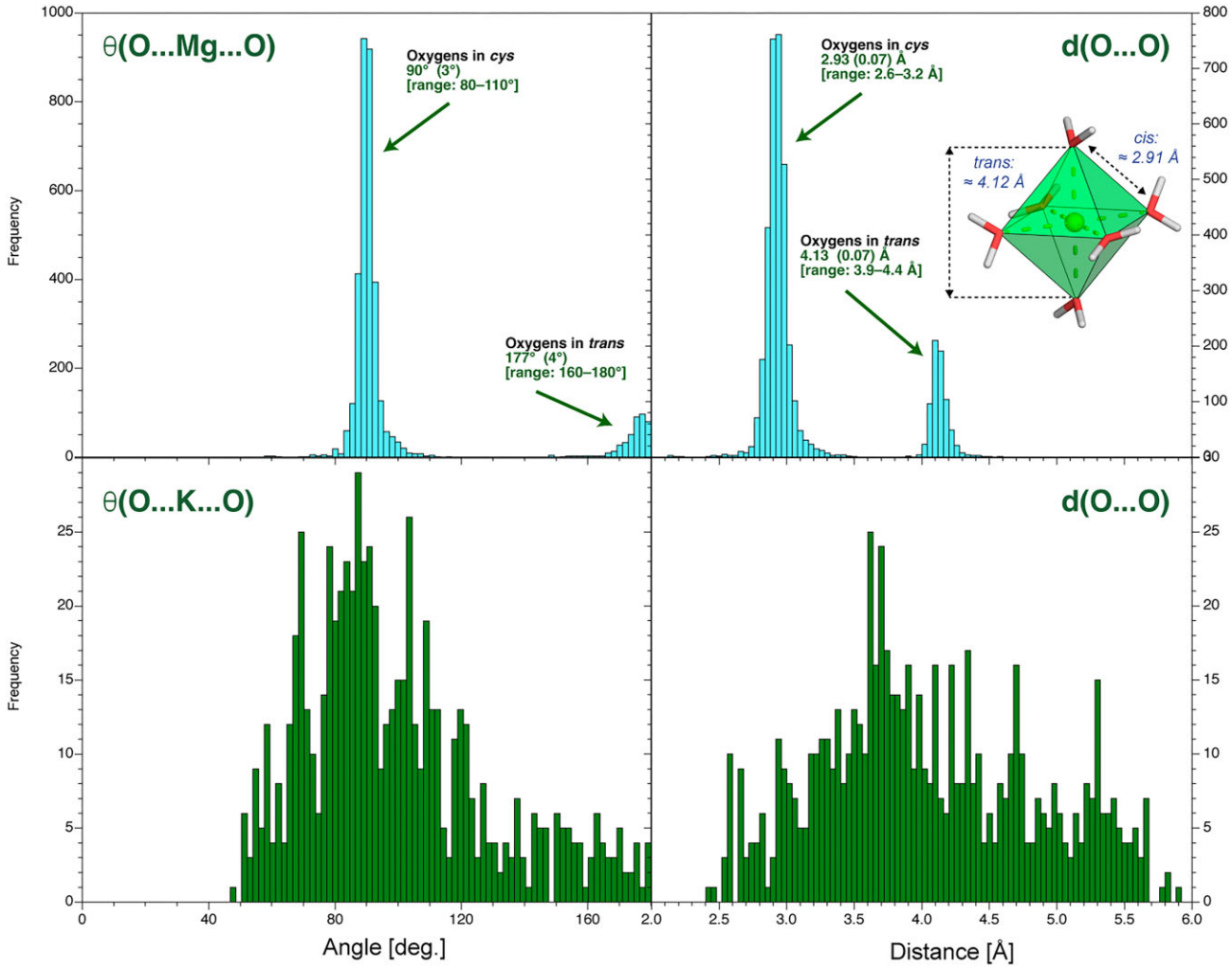

Figure 3. First shell oxygen coordination angle and *d*(O…O) distance histograms for Mg/K derived from the CSD. (**Left**) Coordination angle histograms for θ(O…Mg/K…O) and (**right**) related coordination distances for oxygen ligands in the ion first coordination shell derived from the CSD (49,50). The insert shows an ultra-high-accuracy $Mg(H_2O)_6^{2+}$ X-ray structure showing the water octahedral arrangement around Mg^{2+} (130,131) and the *cis*-/*trans*-configurations. The angle histograms for K are marginaly useful given that the most frequent K ligands in the CSD are diethoxy (O-C-C-O) groups found in crown ethers and cryptands. These groups are rare in nucleic acids except when the cryo-EM/X-ray buffers contains ethylene glycol monomers or PEG fragments (132). Diethoxy groups were excluded from the CSD searches shown Figures 2 and 3.

priately modelled but the experimental density maps were not sufficiently precise to support their assignment. The consistency criteria used to check the K^+ assignments are described in the **SI** which also comprise an EXCEL file listing all 'highly distorted', 'slightly distorted', and 'well-defined' ion-binding sites in the amended 8b0x model.

Results

Amendments made to the 8b0x solvent shell structure

Herein, we assume that the preferred Mg^{2+} coordination number is six in most nucleic acid environments with strict *d*(Mg^{2+}…*O/N*) ≈*2.07/2.19 Å* coordination distances to oxygen, purine N7 and histidine ND1/NE2 nitrogen atoms (Figure 2). Despite its remarkable 1.55 Å resolution, a rapid inspection of the 8b0x structure as deposited to the PDB and of the corresponding *'IonDiagnosis'* file (see **SI**) reveals that only 96 of the 361 assigned Mg^{2+} are hexacoordinated with coordination distances in the 1.9–2.3 Å range.

To establish a comprehensive classification of Mg^{2+}-binding sites, we completed the solvation shells by adding 104 hexacoordinated Mg^{2+} ions to non-assigned density spots. We also added *d*(Mg^{2+}…O/N) ≈2.07/2.19 Å coordination distance restraints during Phenix refinements. Through that process a much clearer solvation shell picture emerged even though additional 'fixes' where necessary. For instance, 28 Mg^{2+} ions with coordination distances in better agreement with those of K^+ were reassigned (Figure 1A). Likewise, two K^+ ions were reassigned as Mg^{2+}.

The coordination of a sub-category of Mg^{2+} ions looked significantly distorted even with the use of distance restraints suggesting that some local density patterns may be too blurred to allow a proper modelling of these sites (see the 'Materials and methods' section). These ions were not included in the 'well-defined' Mg^{2+}-binding site categories described below. However, we included these ions in our amended 8b0x model. For some Mg^{2+}, it was impossible to define a precise hexacoordinated pattern resulting in the deletion of ≈40 of the assigned Mg^{2+} ions or their reassignment to water. It was also necessary

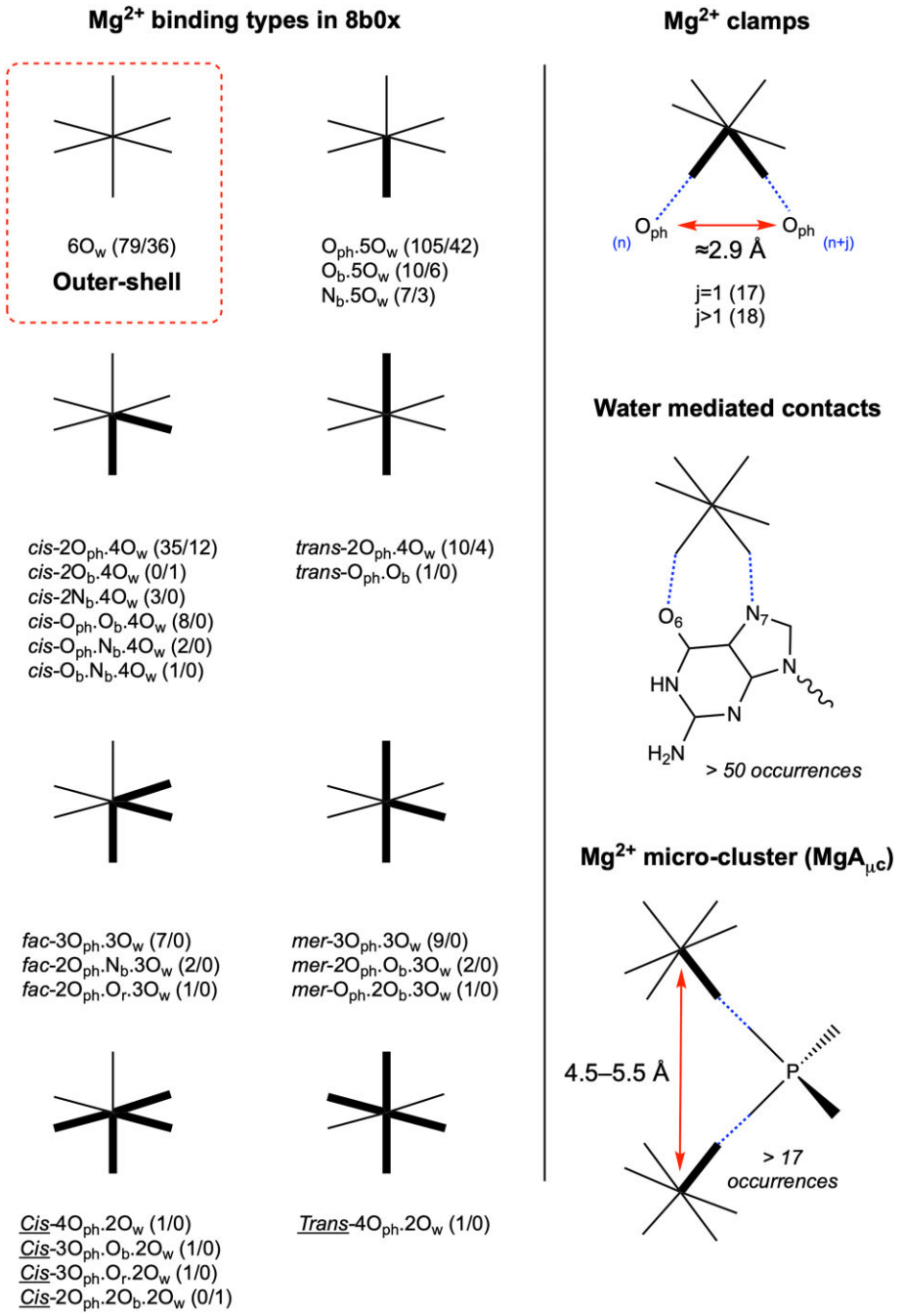

Figure 4. Types and occurrences of Mg^{2+}-binding motifs observed in the amended 8b0x structure. (Left) In addition to the outer-shell $6O_w$-binding motif, all the inner-shell Mg^{2+} ion binding types and occurrences uncovered in 8b0x are shown ('well-defined' and 'not-well-defined' binding site occurrences are given in parenthesis; we did not include binding to r-proteins that account for 15 ions). (Right) The top panel shows a Mg^{2+} clamp where the ion coordinates in *cis*- to two neighbouring (j = 1) or distant (j > 1) O_{ph} atoms. The middle panel shows a $6O_w$ outer-shell binding to a guanine Hoogsteen edge. The bottom panel shows a Mg^{2+} micro-cluster of the $MgA_{\mu c}$ type (see Figure 14).

to alter the upper limit of the Mg^{2+} exclusion zone from 3.6 to 3.4 Å due to the occurrence of specific binding patterns in rRNA not found in the CSD (see **SI**).

To summarize, all densities close to rRNA and r-protein atoms were inspected. We recovered ≈110 Mg^{2+} ions that were either assigned as water molecules, K^+ ions or not assigned at all (Figure 1). This led to a final model that contains 403 Mg^{2+}, 231 K^+ and 21 397 water molecules contrasting with the 361 Mg^{2+}, 168 K^+ and 11 461 water molecules initially assigned. The two models share 299 Mg^{2+} common positions. Although anions can bind to nucleic acids (58,59), we could not identify any of them in 8b0x (see **SI**).

Mg^{2+}-binding site categorization

This ion identification process allowed a clear-cut classification of Mg^{2+} ion-binding sites in terms of type and frequency. Although the resolution of a cryo-EM structure is not uniform and less precise in some regions like the SSU, we considered that the assigned 403 Mg^{2+} ions (290 'well-defined') correspond to an important part of the chelated divalent ions nec-

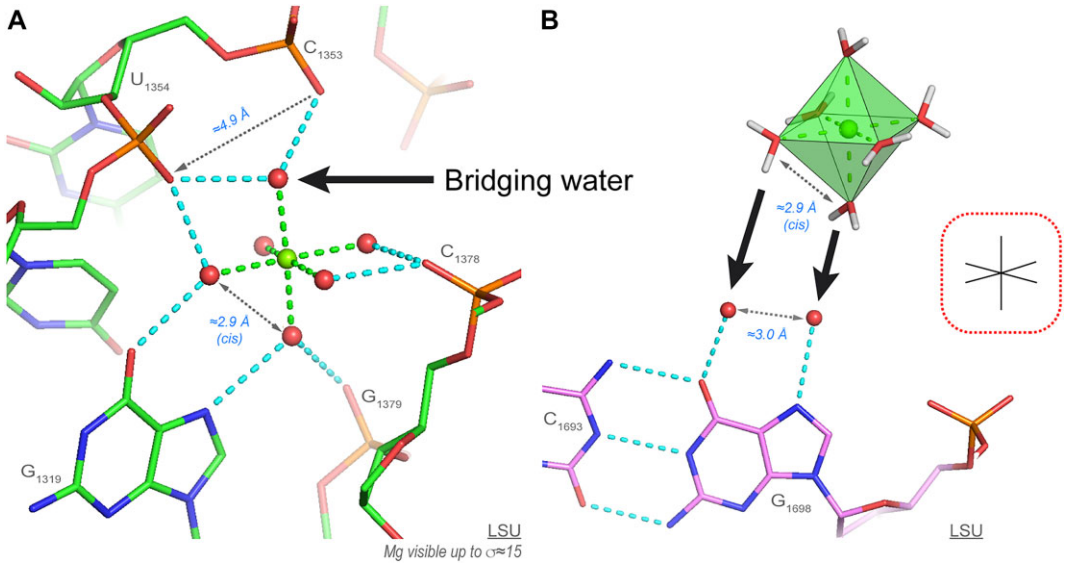

Figure 5. A $6O_w$ ion establishing eight water-mediated contacts to rRNA atoms and a $Mg[H_2O]_6^{2+}$-binding to a guanine Hoogsteen edge. **(A)** This domain 'III' $6O_w$ ion occupies a tight binding pocket where it forms eight water-mediated contacts. Note the binding of two first shell waters to a guanine Hoogsteen edge and the recurrent first shell water bridging two consecutive phosphate groups shown by an arrow. **(B)** Schematics illustrating how two waters bound to a guanine Hoogsteen edge and separated by ≈2.9 Å can be replaced by two first shell waters in *cis*- of a $Mg[H_2O]_6^{2+}$ ion. Green/cyan lines mark distances <2.3 Å and in the 2.6–3.2 Å range. For clarity, experimental densities and some waters were hidden.

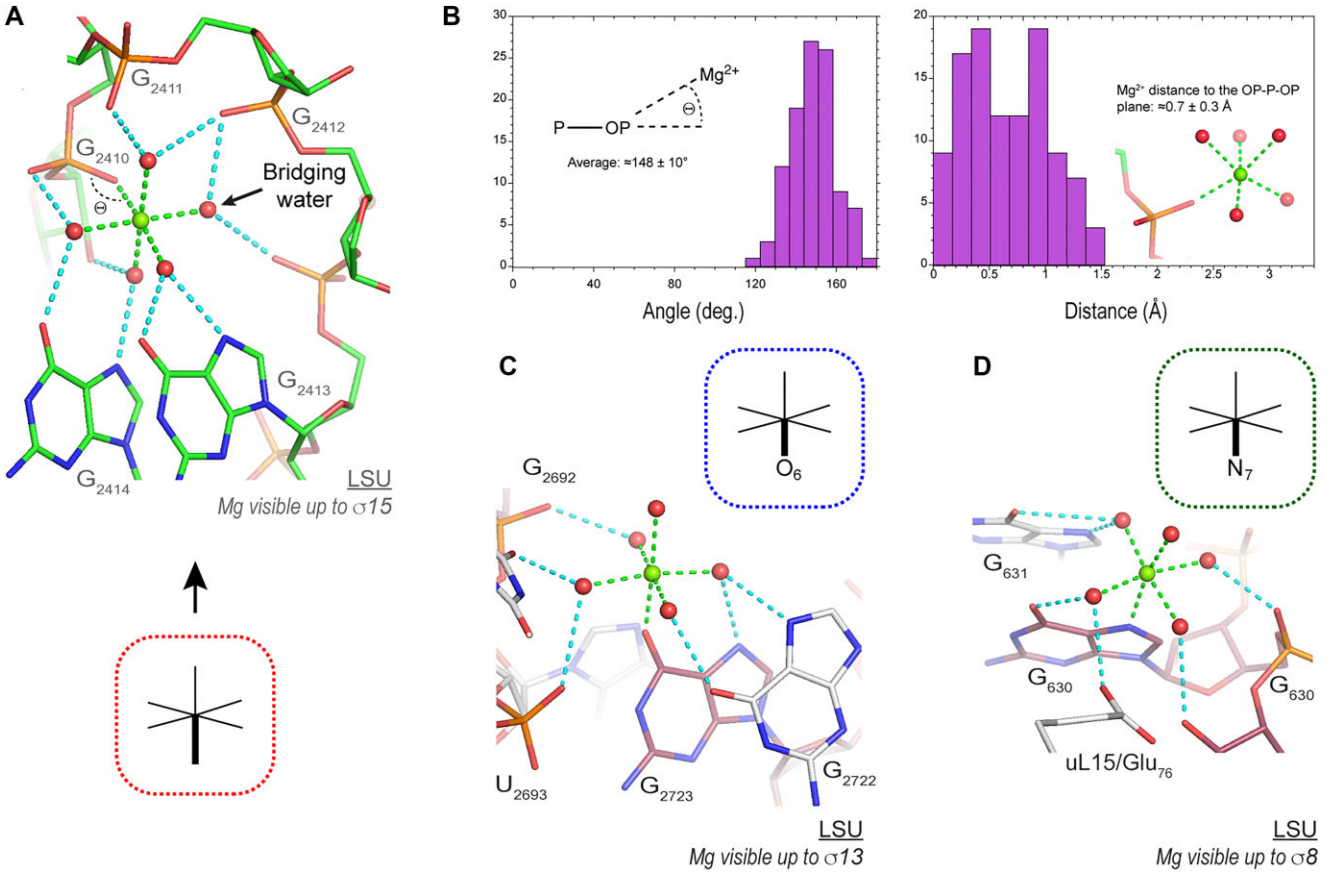

Figure 6. Examples of $O_{ph}/O_b/N_b.5O_w$ Mg^{2+} ions establishing water-mediated contacts to rRNA atoms. **(A)** This domain 'V' $O_{ph}.5O_w$ ion is the most highly connected in 8b0x with one inner-shell and 10 outer-shell contacts. Strikingly, this ion establishes contacts with five consecutive nucleotides and displays at least one bridging water similar to that shown Figure 5A. **(B)** The left histogram illustrates the P–OP…Mg^{2+} angular distribution with the average value calculated from the ensemble of 105 'well-defined' $O_{ph}.5O_w$ occurrences. The right histogram describes the Mg^{2+} distance to the OP–P–OP plane for the same 105 occurrences. **(C)** This domain 'VI' $O_b.5O_w$ ion, although less connected, establishes inner- and outer-shell contacts to two consecutive guanine Hoogsteen edges. **(D)** This domain 'I' $N_b.5O_w$ ion establishes inner- and outer-shell contacts to a guanine Hoogsteen edge and r-protein uL15. Green/cyan lines mark distances <2.3 Å and in the 2.6–3.2 Å range. Experimental densities and some waters were hidden.

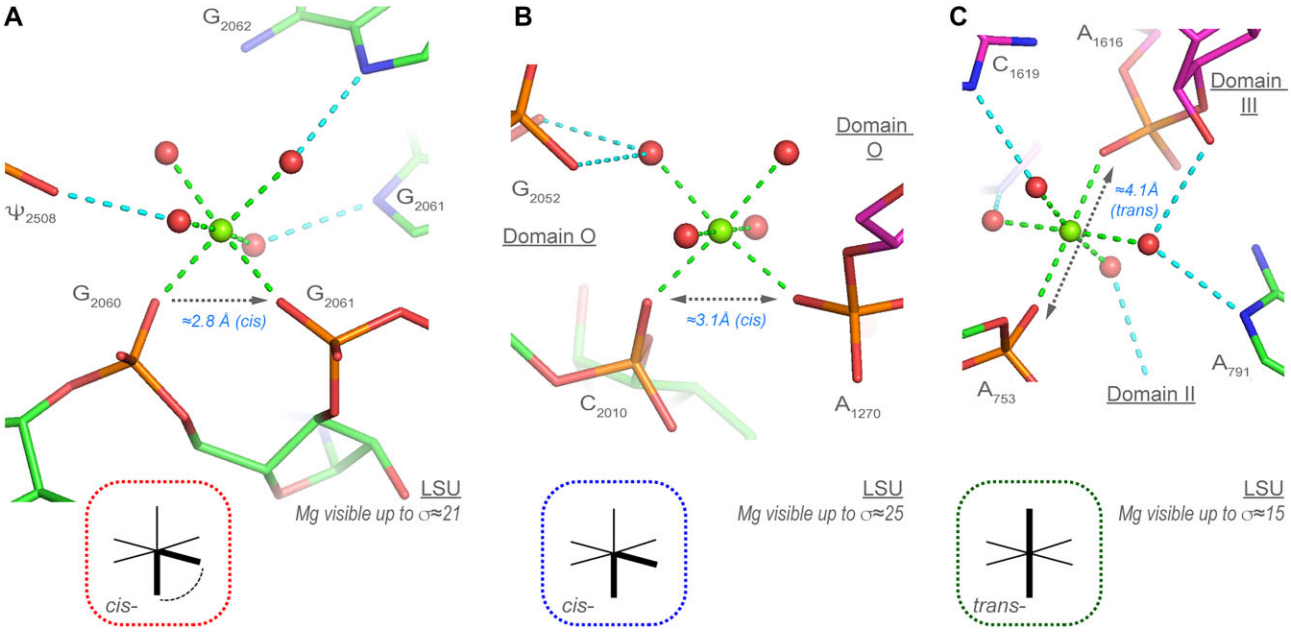

Figure 7. Two *cis*-$2O_{ph}.4O_w$ and one *trans*-$2O_{ph}.4O_w$ motifs. **(A)** Two domain 'V' phosphates form a bidentate Mg^{2+} clamp also defined as a Mg^{2+} 10-membered ring (43,65,67). **(B)** Two non-consecutive phosphates that belong to domain '0' form a *trans*-$2O_{ph}.4O_w$ motif **(C)** Two phosphates form a *trans*-$2O_{ph}.4O_w$ motif; the Mg^{2+} connects domains 'II' and 'III' of the large subunit (LSU). Green/cyan lines mark distances <2.3 Å and in the 2.6–3.2 Å range. Experimental densities and some waters were hidden.

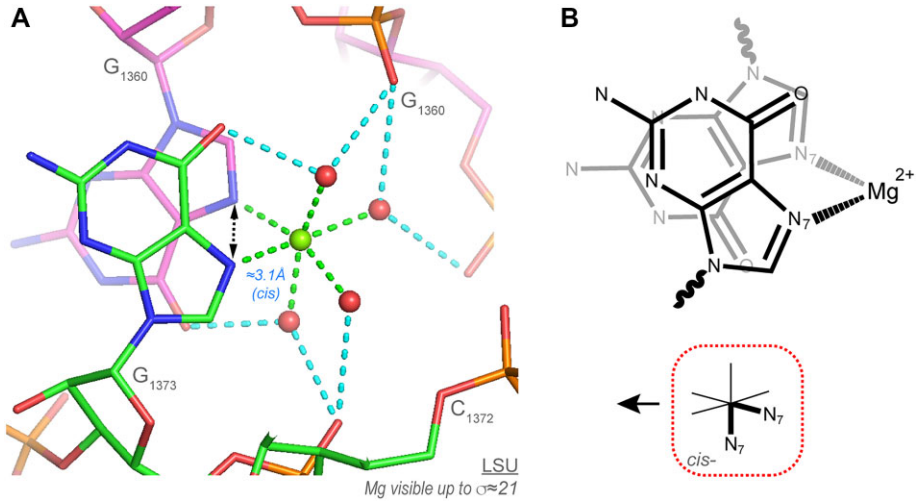

Figure 8. 'Head-to-tail stacked purine' motif. **(A)** Two domain 'III' guanines coordinate a Mg^{2+} through their N7 atoms in a *cis*-$2N_b.4O_w$ arrangement. As a result, a total of nine inner- and outer-shell contacts are formed. The purines in these examples are separated by >10 nucleotides. The two other *cis*-$2N_b.4O_w$ arrangements in 8b0x are shown in Supplementary Figure S3B and C. **(B)** Schematics showing the *cis*-$2N_b.4O_w$ 'head-to-tail stacked purine' arrangement (REF). Green/cyan lines mark distances <2.3 Å and in the 2.6–3.2 Å range. Experimental densities and some waters were hidden.

essary to stabilize a bacterial ribosome. These ions differ from diffuse or weakly chelated ones with no or too weak densities to be characterized in cryo-EM structures. Next, we describe the classification of all the uncovered sites along with their occurrences in the amended 8b0x structure (Figure 4).

• $6O_w$ coordination (79 'well-defined' occurrences among 115): Although $Mg[H_2O]_6^{2+}$ can form up to 12 hydrogen-bonds, the number of water-mediated contacts in 8b0x is in the 1–8 range with an average of ≈4. Here, we considered the 79 'well-defined' ions with density peaks >4.0 and with octahedral angle deviations <10° (see the 'Materials and methods' section). As expected, the best hydrogen bond acceptors are the Hoogsteen (G)O6/(G)N7 atoms and the anionic OP1/OP2 phosphate oxygens that are therefore good binding sites for hexahydrated ions (10,30). Depending on the context, any combination of OP1/OP2/O_b/O_r/N_b atoms can be part of the $Mg[H_2O]_6^{2+}$ coordination shell (see **SI**).

The most strongly bound $6O_w$ ion establishes eight water-mediated contacts to OP/O6/N7 atoms and has likely been trapped during the domain 'III' folding step (Figure 5A). This ion is strongly chelated despite the fact that common knowledge suggests that hexahydrated ions should easily exchange with bulk ions.

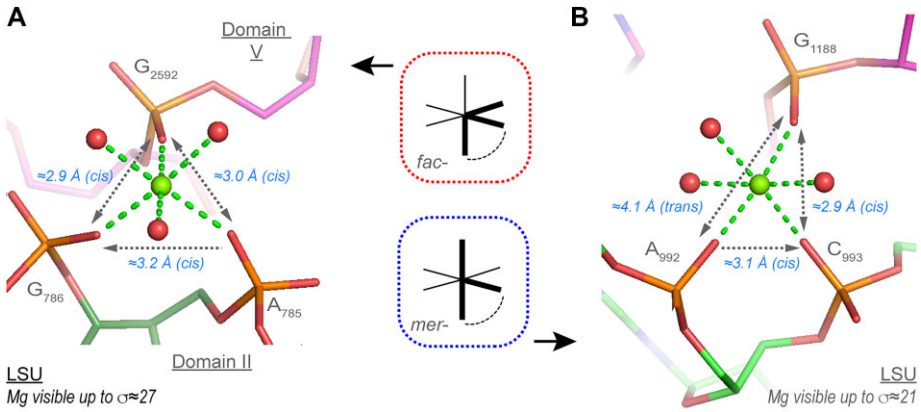

Figure 9. *fac*- and *mer*-3O_{ph}.3O_w-binding sites. **(A)** A *fac*-3O_{ph}.3O_w ion joins domain 'II' and 'V'. **(B)** A domain 'II' *mer*-3O_{ph}.3O_w ion. In both instances, a bidentate Mg^{2+} clamp is associated with a distant third phosphate group. Green/cyan lines mark distances <2.3 Å and in the 2.6–3.2 Å range. Experimental densities and some waters were hidden.

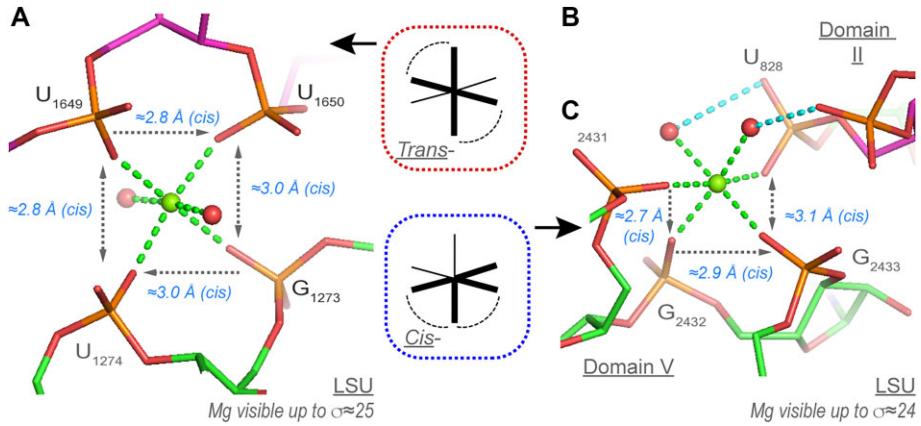

Figure 10. *Trans*- **and** *cis*-**2O_{ph}.4O_w-binding sites. (A)** This 'domain III' *trans*-2O_{ph}.4O_w motif involves two bidentate Mg^{2+} clamps. **(B)** A *cis*-2O_{ph}.4O_w motif connecting domain 'II' and 'V' (the carbons are in green and purple, respectively). The two consecutive bidentate Mg^{2+} clamps form a rare pyramid motif described in (32) that involves three sequential nucleotides. Green/cyan lines mark distances <2.3 Å and in the 2.6–3.2 Å range. Experimental densities and some waters were hidden.

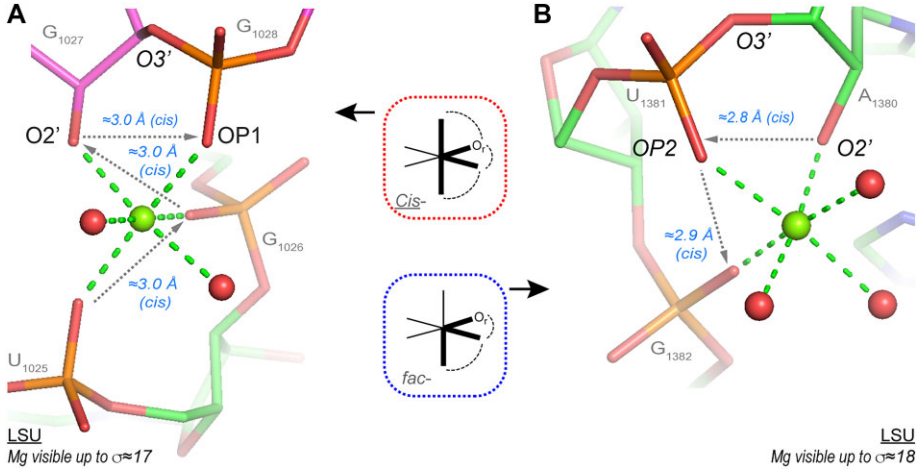

Figure 11. Two rare O2'…Mg^{2+} contacts. **(A)** This domain 'II' *cis*-3O_{ph}.O_r.2O_w motif involves a turn formed by four consecutive nucleotides and a rare backbone conformation leading to a (n)O2'…(n + 1)OP1 distance close to 3.0 Å. **(B)** This domain 'III' *fac*-2O_{ph}.O_r.3O_w ion involves a turn formed by three consecutive nucleotides and a rare backbone conformation leading to a (n)O2'…(n + 1)OP2 distance close to 2.8 Å. The two conformations involving OP1 and OP2 atoms are different. None of the O2' atoms appear deprotonated. Green/cyan lines mark distances <2.3 Å and in the 2.6–3.2 Å range. Experimental densities and some waters were hidden. See also Supplementary Figure S4C.

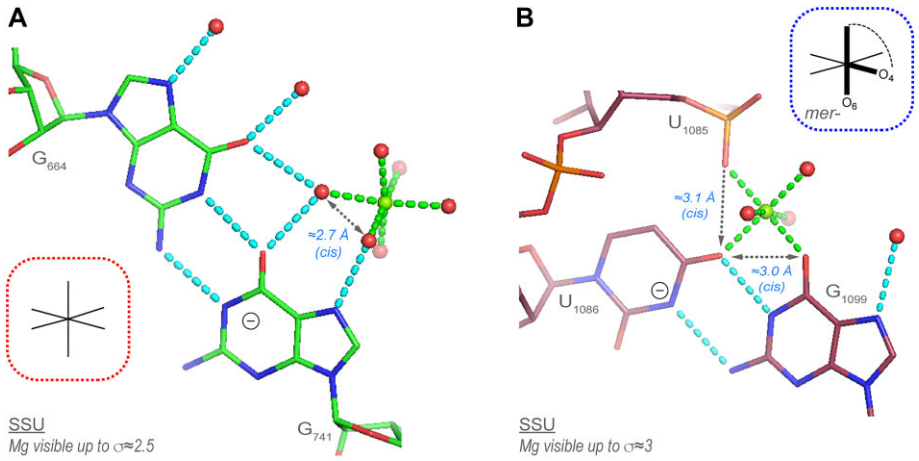

Figure 12. Two Mg^{2+} bound base pairs with a negatively charged guanine/uridine nucleobase. **(A)** The first G•G(-) pair involves a negatively charged guanine nucleobase. The $6O_w$ ion binds to the G(-) Hoogsteen edge (Figure 5). **(B)** The U(-)•G pair involves a negatively charged uridine and is associated with a unique Mg^{2+}-binding pattern of the *mer*-$O_{ph}.2O_b.3O_w$ type. Green/cyan lines mark distances ≤2.3 Å and in the 2.6–3.2 Å range. Experimental densities and some waters were hidden. See also Supplementary Figure S5.

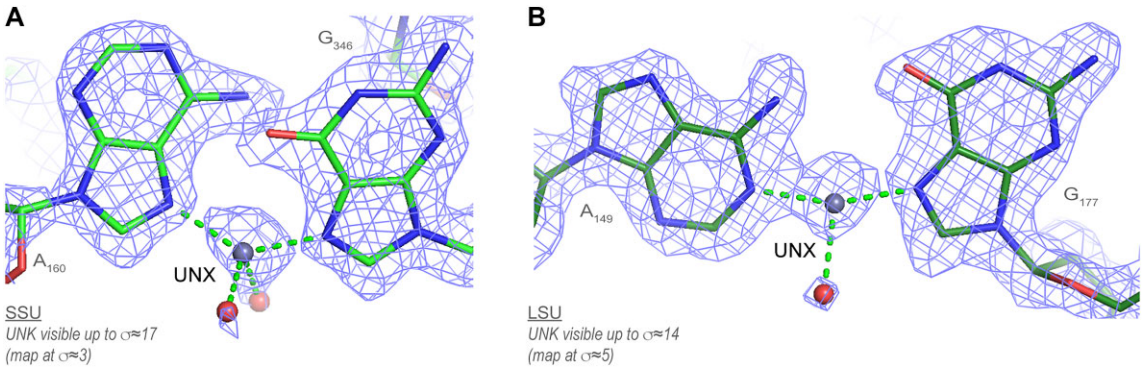

Figure 13. Unexplained ion-binding patterns. **(A)** A UNX atom was placed in a density spot linking the two N7 atoms of an 'A…G' pair that was left empty in 8b0x. UNX corresponds to the PDB code for unknown atom/ion. **(B)** Similarly, a UNX ion was placed in the density linking the **(A)**N1 and the **(G)**N7 atoms that was left empty in 8b0x. It is possible that these UNX ions are Zn^{2+} ions that are compatible with tetrahedral coordination. Green lines mark distances <2.3 Å.

Interestingly, when a $Mg[H_2O]_6^{2+}$ ion establishes water-mediated contacts to a guanine Hoogsteen edge, the two O6/N7-bound water molecules can replace two Mg^{2+}-bound water molecules in *cis*-. This process takes advantage of the similar ≈2.8–3.0 Å distance separating the coordinated guanine and $Mg[H_2O]_6^{2+}$ water molecules and explains why guanine Hoogsteen edges are favourable ion binding sites (Figures 3 and 5B).

- O_{ph} .$5O_w$ coordination (105 'well-defined' occurrences among 147): This is the most frequently observed coordination mode. It involves OP1/OP2 atoms with a slight preference for OP2 atoms (46 versus 59). As for $6O_w$, the coordinated water molecules establish a variable number of water-mediated contacts with rRNA/r-protein atoms. The most highly connected $O_{ph}.5O_w$ ion involves a direct O_{ph} bond to an OP atom completed by 10 water-mediated contacts (Figure 6A). This stunning motif comprises five consecutive nucleotides that wrap around the ion.

When bound to a single phosphate, the (P–OP…Mg^{2+}) angle is ≈148 ± 10° and the bound Mg^{2+} is mainly located in the OP1–P–OP2 plane with an average deviation of ≈0.7 ± 0.3 Å (Figure 6B). We did not observe the elusive 'bidentate' type of coordination (60,61) that implies that Mg^{2+} interacts with both anionic carboxylate or phosphate groups oxygens (Supplementary Figure S1). With 15 binding occurrences, the guanine Hoogsteen edge is, as for $6O_w$ ions, an excellent anchor-point for water-mediated contacts (Figure 6A).

- O_b .$5O_w$ coordination (10 'well-defined' occurrences among 16): These rare patterns involve (G)O6, (U)O4, (PSU)O2 and (C)O2 atoms. Binding to O_b atoms only occurs in rare structural contexts (Figure 6C). An example of a completely encapsulated $O_b.5O_w$ ion was observed in a P4-P6 group I intron structure (15,62). In most instances, the Mg^{2+} ion turns to the Hoogsteen edge. It can also be oriented towards the nucleobase Watson–Crick edge depending on the local environment. The C = O…Mg^{2+} angle is ≈144° with Mg^{2+} strictly in the nucleobase plane while monovalent ions usually are not in the base pair planes (15,63).
- N_b .$5O_w$ coordination (7 'well-defined' occurrences among 10): Coordination to (G/A)N7 but not to N1/N3 atoms was observed (Figure 6D). Coordination to (A)N7 is only observed in higher-order motifs involving more than two-direct contacts (see below). The electron densities around the N7 atoms are often blurred and difficult to interpret as discussed previously (64). Occasionally, direct Mg^{2+} binding to

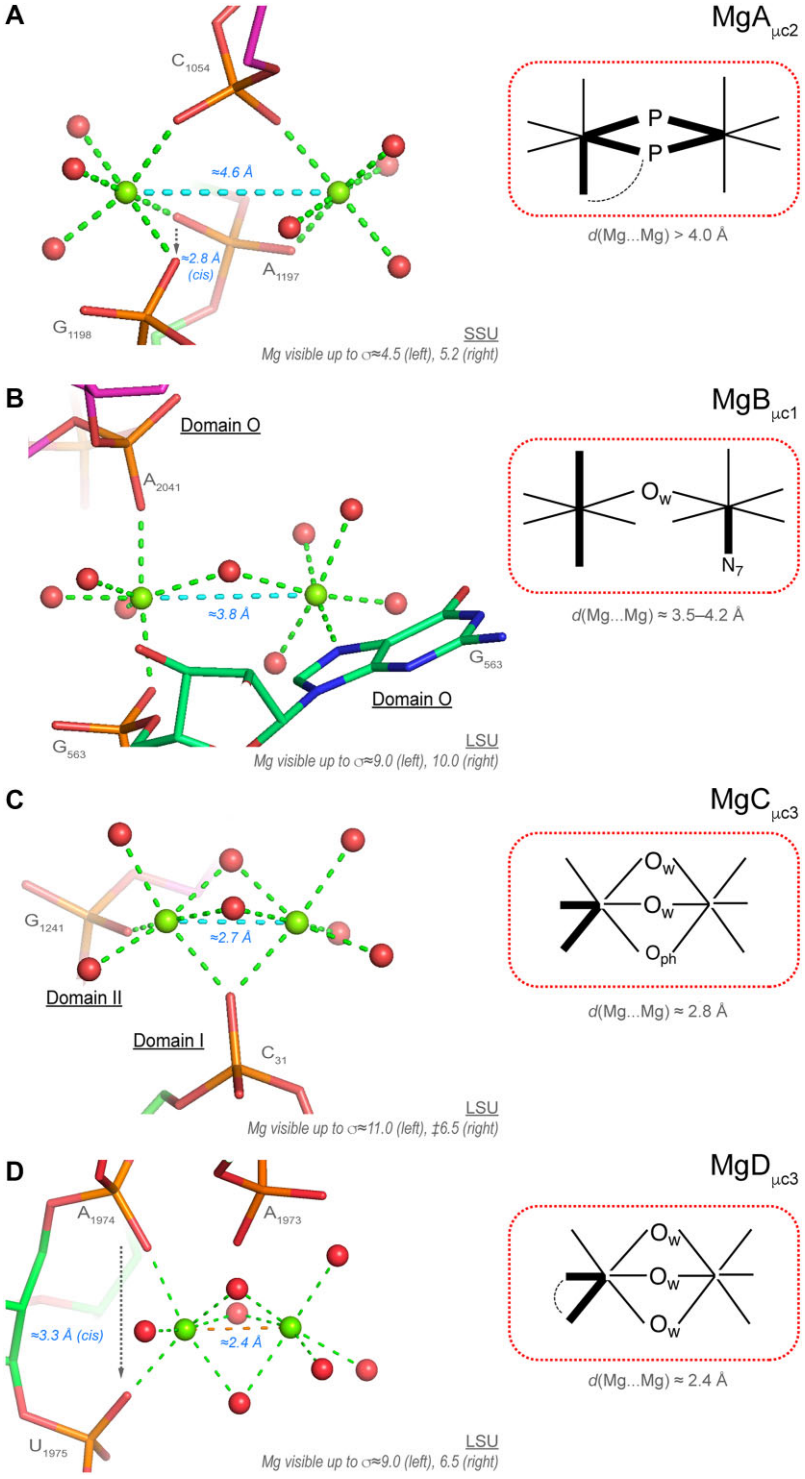

Figure 14. Four types of Mg^{2+}…Mg^{2+} pairs. **(A)** The two bottom phosphate groups of this $MgA_{\mu c2}$ pair belong to adjacent SSU domain '3′C' nucleotides. The first ion is *fac*-$3O_{ph}.3O_w$, the second is *cis*-$2O_{ph}.4O_w$. **(B)** This $MgB_{\mu c1}$ ion pair is located in the central domain 'O'. This ion pair is connected to the same guanine OP2 and N7 atoms and involves a bridging water molecule. The first ion is *trans*-$2O_{ph}.4O_w$, the second is $N_b.5O_w$. **(C)** This $MgC_{\mu c3}$ ion pair connects LSU domains 'I/II'. It involves two bridging waters and an O_{ph} atom associated with a short 2.7 Å inter-metal distance (see also Supplementary Figure S6C and D). The first ion is *cis*-$2O_{ph}.4O_w$, the second is $O_{ph}.5O_w$. **(D)** In the absence of corroborating examples, this domain 'IV' $MgD_{\mu c3}$ ion pair with a short 2.4 Å inter-metal distance must be considered with caution. The first *cis*-$2O_{ph}.4O_w$ ion forms a bidentate phosphate clamp, the second is $6O_w$. For densities, see Supplementary Figure S6E and F). Green/cyan lines mark distances <2.3 Å and inter-metal distances. Experimental densities and some waters were hidden.

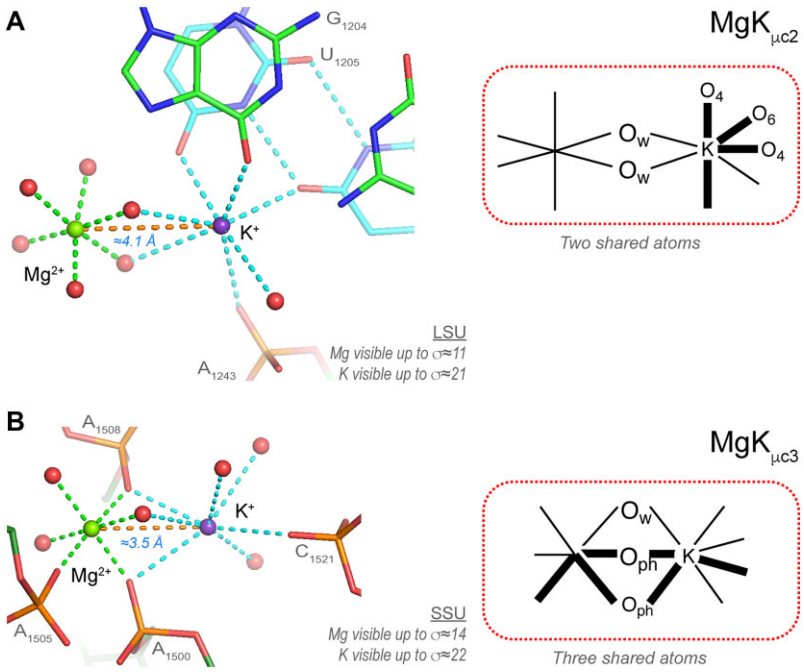

Figure 15. Mg^{2+}…K^+ pairs with two and three bridging water molecules. **(A)** This $MgK_{\mu c2}$ pair involves a Mg^{2+} of the $6O_w$ type and a heptacoordinated K^+ that binds to the deep groove of a domain 'II' G•U pair (carbon atoms in cyan). Two water molecules are bridging the ions. **(B)** This domain 'III' $MgK_{\mu c3}$ pair displays a shorter inter-metal distance. It involves a Mg^{2+} of the *mer*-$3O_{ph}.3O_w$ type and a heptacoordinated K^+ (for density representations, see Supplementary Figure S7). Three water molecules are bridging the ions. Green/cyan lines mark distances ≤2.3 Å and in the 2.6–3.2 Å range; orange lines mark inter-metal distances. Experimental densities and some waters were hidden.

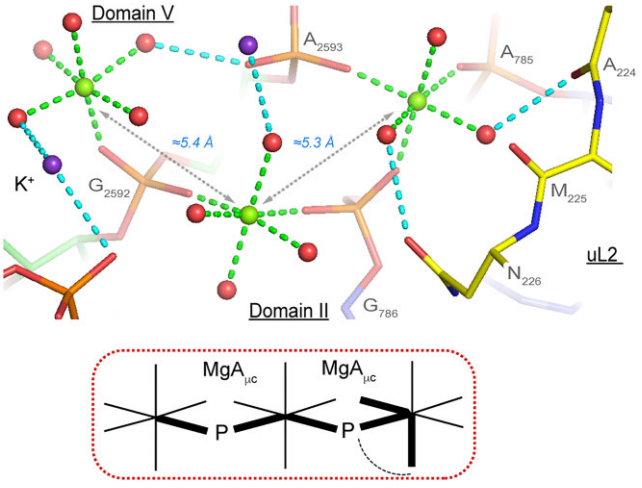

Figure 16. Partial view of the LSU/uL2 interface centred on two $MgA_{\mu c}$'s. This view illustrates the intricacy of the ion-binding patterns at the LSU/uL2 interface that involves the $MgA_{\mu c}$ named D2 by Williams and co-workers (6,43,80). These ions link the LSU domains 'II/V' with a N-terminal uL2 segment (yellow backbone). It can be hypothesized that the Mg^{2+} ions first link the two distant domains 'II' and 'V'. When this connection is established, uL2 can bind. K^+ ions (purple) are present at the interface. Green/cyan lines mark distances <2.3 Å and in the 2.6–3.2 Å range. Experimental densities and some waters were hidden.

N7 atoms was considered important for catalytic mechanisms (16,65,66).

• *Cis-* $2O_{ph}.4O_w$ coordination and variations (35 'well-defined' occurrences among 47): *Cis*-$2O_{ph}.4O_w$ coordination modes can be split into two main categories involving consecutive (17 occurrences) and sequence distant nucleotides (18 occurrences). The first category (Figure 7A) comprises bidentate Mg^{2+} clamp motifs (30,43,65,67). These motifs, also defined as 10-membered ring systems (Mg^{2+}…OP–P–O5'–C5'–C4'–C3'–O3–P–OP), involve any combination of OP1/OP2 atoms with a preference for the deep groove OP2/OP2 atoms. Other patterns comprise O_{ph} atoms from distant residues (Figure 7B). A few clamps involving a Mg^{2+} bridging an $O_{ph}(n)$ and an $O_{ph}(n + 2)$ atom also occur. These clamps were considered as new motifs and called 16-membered ring systems but are simply a variation of the 10-membered ring system (32).

Importantly, there is a strict correspondence between the distance separating two Mg^{2+} first shell water molecules in *cis*- and the ≈2.9 Å distance separating two coordinated O_{ph} atoms (Figures 3 and 7A). Thus, Mg^{2+} ions stabilize short O_{ph} contacts with $d(O_{ph}…O_{ph})$ <3.4 Å. This distance range is associated with the Mg^{2+} first shell water molecules in a *cis*-configuration. As discussed below, all short $d(O_{ph}…O_{ph})$ ≈2.9 Å distances observed in 8b0x are stabilized directly or indirectly by a Mg^{2+} ion (for stabilization through both, direct and water-mediated contacts, see Supplementary Figure S2). The *cis*-$2N_b.4O_w$-binding sites are discussed below. Variations of these patterns with O_b/N atoms replacing O_{ph} atoms are discussed in the **SI**.

• *Cis-* $2N_b$ $.4O_w$ coordination (three 'well-defined' occurrences): One SSU and two LSU *cis*-$2N_b.4O_w$ patterns involving non-consecutive N7 atoms were observed. They engage G/G or A/G nucleotide pairs (Figure 8 and Supplementary Figure S3) and were named elsewhere as 'purine N7 seats' (15,30). However, it might be more appropriate to name them 'head-to-tail stacked purine' motifs (Figure 8 and Supplementary Figure S3). Each of these ions bind to two

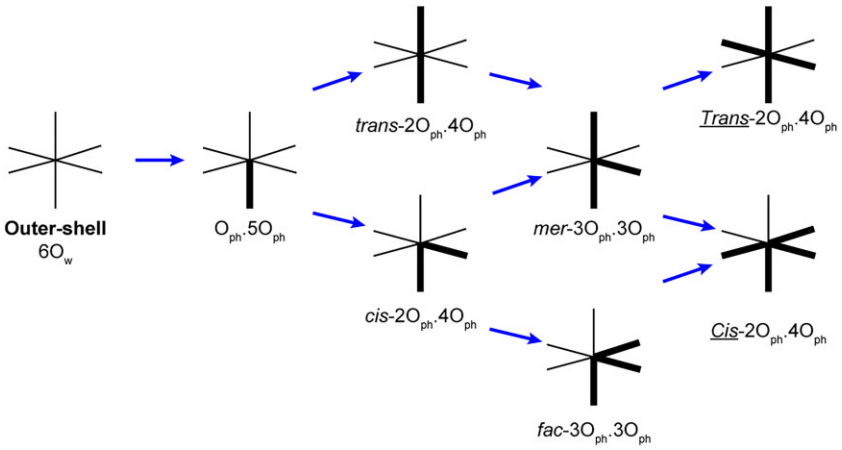

Figure 17. Sketch describing the dehydration hierarchy of Mg^{2+}-binding motifs. Illustration of the path for going stepwise from an hexahydrated ion towards more complex RNA-binding motifs.

N7 atoms and these ions are also coordinated through water-mediated contacts to three or four OP2 atoms. In total, they are involved in 8–9 inner- and outer-shell contacts. This rare motif, involved in the folding and stabilization of specific rRNA fragments, is recurrent in ribosomes from various kingdoms (16,30).

Some of us questioned earlier the nature of the ion associated with the *cis*-2N$_b$.4O$_w$ motif and suggested that the assigned Mg^{2+} may be an hexahydrated Zn^{2+} given the very high-density peaks observed in some X-ray structures and the affinity of Mg^{2+} for purine N7 atoms that is much lower than that of Zn^{2+} (16,51). At this stage, this hypothesis cannot be excluded and Zn^{2+} might be present at similar locations in rRNA as an eventual contaminant (see below). The hypothesis of hexacoordinated Zn^{2+} replacing hexacoordinated Mg^{2+} ions at histidine containing sites as been discussed elsewhere (68).

- *Trans-* 2O$_{ph}$ .4O$_w$ coordination and variations (10 'well-defined' occurrences among 14): These patterns are less frequent than the *cis-* patterns. They are more difficult to characterize given d(O$_{ph}$…O$_{ph}$) ≈4.2 Å that overlap with other similar d(O$_{ph}$…O$_{ph}$) distances (Figures 3 and 3C). Although, their architecture implies a greater flexibility when compared to *cis-* patterns. Variations of this motif involving the replacement of one or two O$_{ph}$ atom(s) by O$_b$/N$_b$ atoms are rare (see Supplementary Figure S2A).
- *fac-* 3O$_{ph}$ .3O$_w$ and *mer-* 3O$_{ph}$ .3O$_w$ coordination and variations (22 'well-defined' occurrences among 23): The 3O$_{ph}$.3O$_w$ coordination type comprises 7 *fac-* and 9 *mer-* arrangements that are likely formed during ribosome biogenesis. Most of these occurrences feature a Mg^{2+} bidentate motif (Figure 9) with only one exception in the SSU. There, the bidentate motif involves a two-nucleotide insertion. Variations of these motifs are mentioned in the **SI**.
- *Cis-*/*trans-* 4O$_{ph}$ .2O$_w$ coordination and variations (five 'well-defined' occurrences among eight): We observed five 'well-defined' LSU-binding sites in addition to three 'poorly-defined' ones: two in the SSU and one in the uS2 r-protein region. For naming these binding sites, we used the *cis-*/*trans-* configuration of the two bound water molecules (for nomenclature details, see the 'Materials and methods' section). The first binding site is *trans*-4O$_{ph}$.2O$_w$. Here, all four O$_{ph}$ atoms are coplanar with Mg^{2+} (Figure 10A). The second is *cis*-4O$_{ph}$.2O$_w$ (10B). This domain 'V' site displays a unique pattern of three consecutive nucleotides that is completed by a fourth domain 'II' phosphate group.

These intricate motifs mostly based on Mg^{2+} bidentate chelation are rare given the complexity of the folds and the difficulty in dehydrating multiple times a $Mg[H_2O]_6^{2+}$ ion. Such motifs can only emerge in large RNAs where the nucleotide chain can fold back on itself as for instance in the ≈440 nucleotide long P4-P6 group I intron (PDBid: 8tjx; res. 2.44 Å) where a *trans* -4O$_{ph}$.2O$_w$ motif involving nucleotides (n, n + 2, n + 3, n + 4) is observed (69). It is expected that additional variations of these motifs will be identified. Variations of these patterns are discussed in the **SI**.

Rare inner-shell Mg^{2+}-binding to O2′ atoms

Three 'well-defined' Mg^{2+}…O2' contacts were characterized (15). Two of those involve a bidentate contact to OP1/OP2 atoms where the O2' atom is at 3.0/2.8 Å from the OP1/OP2 atoms of the next residue (Figure 11). Only two O2'(n)…OP1/OP2(n + 1) contacts of the Mg^{2+}…O2'-C2'-C3'-P-OP…Mg^{2+} (a six-membered ring) were localized in the entire 70S suggesting that these configurations need the presence of Mg^{2+} ions. The first binding type is *cis*-3O$_{ph}$.O$_r$.2O$_w$. It is the only binding site that involves a chain of four consecutive nucleotides (Figure 11A). The second is *fac*-2O$_{ph}$.O$_r$.3O$_w$ and comprises three consecutive nucleotides (Figure 11B). The third contact of the O$_r$.5O$_w$ type needs to be validated through the analysis of larger structural ensembles (Supplementary Figure S4C). Overall, these occurrences imply that in rare structural contexts, O2' atoms coordinate to Mg^{2+}. Two of these motifs induce turns associated with successive nucleotides that are probably impossible to achieve, like bidentate binding in general, without the participation of Mg^{2+} ions. None of the two O2' atoms are deprotonated since one of them is hydrogen bonded to a (C)OP2, the other to a (G)N7 atom.

Anionic base pairs in 8b0x

According to a recent study (70), at least four anionic base pairs are conserved in bacterial ribosomes. In 8b0x, two and one cWW U(-)•G pairs are in the SSU and LSU, while a fourth cWW G•G(-) pair is in the LSU (Figure 12 and

Supplementary Figure S5). These pairs involve a deprotonated uridine/guanine nucleotide that carries a negative charge.

One of these U(-)•G pairs displays a unique Mg^{2+}-binding pattern of the *mer*-$O_{ph}.2O_b.3O_w$ type (Figure 12B). These pairs involving negatively charged nucleobases are unique in the ribosomal ecosystem. Besides, we note the occurrence of an [A^+•C]•ho5C base triple (Supplementary Figure S5) associated with a ho5C base modification assigned as a C nucleobase in *E. coli* PDB structures (71).

Unexplained 'metal' binding patterns

While most well-ordered 8b0x ion-binding sites could be assigned as Mg^{2+}/K^+ ions, two density peaks were not associated with these ions (Figure 13). In the SSU, an unidentified ion links the two N7 atoms of a 'metal-mediated' A…G pair (Figure 13A). This position with a density peak distant by ≈2.1 Å from the two N7 atoms can only be occupied by a tetrahedral ion such as Zn^{2+}. However, there is no clear-cut evidence for a Zn^{2+} assignment. Therefore, we placed a UNX ion with a $2N_b.2O_w$ coordination in our model, UNX being the PDB code for an unknown atom/ion.

In the LSU, another 'metal-mediated' A…G pair is observed. A density peak is seen between the (A)N1 and the (G)N7 atoms with both nucleobases being strictly coplanar (Figure 13B). This pattern looks like that of documented Ag, Hg or Au metal-mediated base pairs (41,72–74). Such base pairs have not been observed in the 7k00 *E. coli* ribosome used to build the 8b0x model. In the later structures, the adenine is shifted to establish a (A)N6…N7(G) hydrogen bond. Since Mg^{2+}/K^+ and water molecules cannot occupy such locations, these unusual base pairs suggest the presence of metal contaminants that are not present in other ribosomal structures or of excess Zn^{2+} ions that are difficult to identify through conventional techniques (75). We mentioned above and elsewhere the possible association of Zn^{2+} ions with the $2N_b.4O_w$ motifs (16). This hypothesis has neither been confirmed nor invalidated. The inclusion of molecules not added to the buffer are sometimes observed in cryo-EM structures as is the case for two polyamines mentioned in a recent 1.9 Å resolution *Human* 80S structure (76).

Mg^{2+}…Mg^{2+} ion pair occurrences and classification

The occurrence Mg^{2+}…Mg^{2+}, Mg^{2+}…K^+ and K^+…K^+ ion pairs is an intriguing feature of the ribosomal ionic shell. Although similar ion pairs have been observed in nucleic acids and in protein systems (60,77–79), their characteristics are rarely discussed unless they are located in catalytic sites. In this study, an ion pair is defined by two metals sharing at least one and up to three phosphate groups, oxygen atoms or water molecules. For all pairs, Mg^{2+} ions are hexacoordinated. None of these pairs are associated with r-proteins.

Here, we propose a preliminary classification of Mg^{2+}…Mg^{2+} pairs. We divided the observed Mg^{2+}…Mg^{2+} pairs into four categories called micro-clusters or Mg^{2+}-µc's (2,6,43,80). The $MgA_{µc}$ involves two Mg^{2+} ions that are separated by >4.2 Å and bridged by at least one phosphate group. The $MgB_{µc}/MgC_{µc}/MgD_{µc}$ clusters display shorter inter-metal distances in the 4.2–2.4 Å range. In these groups, the metals share from one to three oxygen atoms and/or phosphate groups. To differentiate them, we added to their designation a 1–3 suffix. Thus, the cluster shown Figure 14A is named $MgA_{µc2}$ since the Mg^{2+} ions share two PO_4 groups.

- Type I 'magnesium micro-clusters' ($MgA_{µc}$): Mg^{2+}…OP-P-OP…Mg^{2+} with $d(Mg^{2+}…Mg^{2+})$ ≈4.5–5.3 Å (17 'well-defined' occurrences). In $MgA_{µc}$, the ions can share one (as in $MgA_{µc1}$) or two (as in $MgA_{µc2}$) phosphate group(s) (Figure 14A and Supplementary Figure S6A). These arrangements, previously called Mg^{2+}-µc (2,6,43,80), resemble the bridges formed by carboxylate groups between two metal ions in enzymatic systems (60). In rRNA, such $MgA_{µc}$ were considered to be part of the peptidyl transferase centre (PTC) of ribosomes from all kingdoms and were also found in the P4–P6 domain of the tetrahymena group I intron ribozyme (81) and the self-spliced group II intron from *Oceanobacillus iheyensis* (82) among other RNA structures.
- Type II ($MgB_{µc}$): Mg^{2+}…O_w…Mg^{2+} with $d(Mg^{2+}…Mg^{2+})$ ≈3.8 Å (two 'well-defined' occurrences). In the firstpair ($MgB_{µc1}$), the ions share a single water molecule (Figure 14B). The ions of the second pair share also one water molecule. The presence of an alternate hydration pattern is suggested by two water molecules separated by 2.07 Å. This ion pair must be interpreted with caution (Supplementary Figure S6B).
- Type III ($MgC_{µc}$): Mg^{2+}…O_w…Mg^{2+} with $d(Mg^{2+}…Mg^{2+})$ ≈2.8 Å (two 'well-defined' occurrences). Both ions of a first pair ($MgC_{µc3}$) share an OP1 atom and two water molecules (Figure 14C). The ions of a second pair ($MgC_{µc3}$) share three water molecules (Supplementary Figure S6C). These pairs are reminiscent of a documented Mg^{2+}…Mg^{2+} ion pair where the ions are separated by 2.7 Å (Supplementary Figure S6D). The later pair appears in a structure of a 5S rRNA Loop E fragment at 1.5 Å resolution (79). Previously, we proposed that such an arrangement resulted from alternate conformations of two close Mg^{2+}-binding patterns (83). However, given the two identified $MgC_{µc3}$ pairs in 8b0x, we re-evaluated this hypothesis. Our data suggest that in specific environments, pairs with $d(Mg^{2+}…Mg^{2+})$ ≈2.8 Å can be stabilized by their environment. This is supported by a recent CSD structure showing a similar Mg^{2+} pair (84), by descriptions of inorganic compounds with stable Mg(I)…Mg(I) covalent bonds with $d(Mg^+…Mg^+)$ ≈2.8 Å and by implications of Mg pairs in enzymatic systems (85,86).
- Type IV ($MgD_{µc}$): Mg^{2+}…O_w…Mg^{2+} with $d(Mg^{2+}…Mg^{2+})$ = 2.38 Å (one 'well-defined' occurrence). Here, the two Mg^{2+} ion proximity is astonishing (Figure 14D). This ion pair ($MgD_{µc3}$) involves three bridging water molecules associated with surprisingly well-defined density patterns and resembles the ones described in Supplementary Figure S6E and F. The first Mg^{2+} is of the *cis*-$2O_{ph}4O_w$ type; the second involves a deformed $6O_w$ coordination octahedron. Additionally, a Mg pair with $d(Mg^{2+}…Mg^{2+})$ ≈2.42 Å has been described in a 1.52 Å resolution nuclease structure where one of the ions is not hexacoordinated (87). Independent observations need to confirm the existence of ion pairs with $d(Mg^{2+}…Mg^{2+})$ <2.50 Å.

Mg^{2+}…K^+ ion pairs (28 'well-defined' occurrences among 42)

Given the exceptional 8b0x resolution, over 200 binding occurrences of K^+ ions to rRNA atoms were characterized. Among those, 28 'well-defined' Mg^{2+}…K^+ pairs with $d(Mg^{2+}…K^+)$ ≈3.5–4.4 Å were identified. In many instances, the K^+ ions share two water molecules ($MgK_{µc2}$) with Mg^{2+}

(Figure 15A). A subcategory of these pairs involves 10 occurrences of a K^+ ion bound to the deep groove of G•U pairs. Seven of these pairs are associated with a Mg^{2+} of the $6O_w$ type. A less frequent pattern where Mg^{2+} and K^+ share three oxygen atoms ($MgK_{\mu c3}$) involve shorter inter-metal distances (Figure 15B). In all instances, the K^+ density peak is significantly higher than that of the Mg^{2+} ion and of their surrounding water molecules (Supplementary Figure S7).

Mg^{2+} ions are rarely present at the SSU/LSU interface

Among the 408 Mg^{2+} ions in 8b0x, only a single $O_{ph}.5O_w$ Mg^{2+} ion contacts both subunits (Supplementary Figure S4A). Hence, Mg^{2+} ions are rarely present at the SSU/LSU interface and are therefore not of importance for the subunit assembly. The presence of a single Mg^{2+} ion at the SSU/LSU interface might result from the high Mg^{2+} buffer condition. Overall, this suggests that destabilization of the 70S particles observed at low Mg^{2+} concentrations is the result of the destabilization of each of the subunits leading to a fuzzy structural interface (7,88). On the other hand, the association of ribosome particles forced by Mg^{2+} concentrations >15 mM may result from subunit stabilization rather than from the presence of interfacial Mg^{2+} ions (3).

Mg^{2+} bound to r-proteins are uncommon

Only one poorly defined *cis*-$3O_{coo}.2O_w.N_{His}$ binding site buried in uS2 was observed (Supplementary Figure S4B). This binding site is also present in the parent 8fto structure. No other r-protein binding site was characterized suggesting that r-proteins might have evolved to avoid competition for Mg^{2+} resources with rRNA. Overall, the need for Mg^{2+} to support proper r-protein functions is significantly smaller than that required by RNA. We note that this motif involves a 'carboxyl clamp' alike the phosphate clamps shown Figure 7.

Mg^{2+} ions at rRNA/r-protein interfaces

Mg^{2+} ions are also observed at rRNA/r-protein interfaces (Supplementary Table S1 and **SI**). Five of these ions make direct contacts to rRNA and r-proteins while others form at least one direct contact with the rRNA and form water-mediated contacts with the r-proteins.

Eight ions are located at the LSU/uL2 interface of the PTC, which contains the largest number of observed contacts (10,43,80). Williams and co-workers noted the conservation of a Mg^{2+}-μc at this interface involving an 18 amino acid-long N-terminal loop and discussed the importance of the Ala-Met-Asn sequence in the ribosomal assembly process (Figure 16). This interface is conserved across Archaea, Bacteria and Eukarya (80). There, the involved Mg^{2+} ions establish direct contacts through $MgA_{\mu c}$'s binding to RNA phosphate groups but only form water-mediated contacts to uL2. This suggests that Mg^{2+} first stabilizes the local RNA folds allowing subsequent binding of uL2. A more detailed discussion of the rRNA/r-protein interfaces is beyond the scope of this paper.

Mg^{2+} linking LSU domains

A total of 20 out of the 21 'well-defined' Mg^{2+} ions coordinate with LSU domains through a combination of direct and water-mediated contacts (Supplementary Table S2 and Figures 7, 9–11, 14 and 16). As previously described, a few of these involve Mg^{2+}-μc's motifs (6,43,80). Interestingly, Mg^{2+} contacts linking SSU domains were not observed suggesting a less complex folding process for this subunit. Among the characterized intra-LSU links, seven of them involve domain 'II/V', none involve domain 'VI' and only two are associated with domain 'III'. As a result, the largest number of LSU contacts link domain 'II/V' as well as domain 'V' and r-protein uS2 (Figure 16). The later contacts were discussed by Williams and colleagues (6,43,80).

Description of a universal set of rules to identify Mg^{2+}-binding sites

From the examination of the amended 8b0x structure, we inferred straightforward binding rules. We will discuss these rules step by step starting from those related to Mg^{2+} bidentate motifs.

Locating $Mg^{2\pm}$ bidentate clamps (O_{ph} …O_{ph}): A unique feature of Mg^{2+}-binding clamps is associated with a conserved O_{ph}…O_{ph} distance close to ≈2.9 ± 0.2 Å. This distance matches that separating Mg^{2+} water molecules in *cis*- (see Figures 3, 7, 9–11 and 14). Hence, we hypothesized that a simple method to locate Mg^{2+} bidentate clamps is to screen all O_{ph} pairs with $d(O_{ph}…O_{ph})$ <3.4 Å. By discarding the poorly modelled O_{ph} pairs comprising at least one O_{ph} atom with B-factors >60 $Å^2$, we located a total of 94 pairs (87 'well-defined' ones) involving 36 OP1…OP1, 23 OP2….OP2 and 35 OP1…OP2 combinations. All 94 pairs were associated with Mg^{2+} and 92 of them form Mg^{2+} bidentate clamps. Two remaining motifs display a distinctive Mg^{2+} water-mediated contact stabilizing the short $d(O_{ph}…O_{ph})$ ≈2.9 Å distance (Supplementary Figure S2). We suggest that the latter motifs correspond to intermediates in the formation of Mg^{2+} bidentate clamps.

We concluded that all *cis*-bidentate motifs involving a Mg^{2+} ion can be detected in rRNA fragments of appropriate resolution by screening $O_{ph}…O_{ph}$ distances ≤3.4 Å. All 'higher-order' patterns of the *fac-*/*mer-*/ *cis-*/*t rans-* type can also be localized by tracing these distances since most of them involve at least one Mg^{2+}*cis*-bidentate motif. The only exceptions are the less frequent motifs in *trans-* that cannot be detected through this technique (Figure 7C). As a result, the 94 uncovered *cis*-binding modes involve a limited number of 68 'well-defined' Mg^{2+} ions that are all associated with critical rRNA-folding patterns.

To further emphasise the effectiveness of this stereochemical rule, we checked the O_{ph} pairs with $d(O_{ph}…O_{ph})$ ≤3.4 Å and could identify seven new Mg^{2+} bidentate motifs not assigned in the initial 8b0x structure. This illustrates the ability of this criterion to help characterize Mg^{2+}-binding sites that escaped from the experimentalist's attention. It also suggests that this criterion is universal and can be applied to the search of major Mg^{2+}-binding sites in all RNA systems as well as in proteins where the main Mg^{2+} ligands are carboxylate groups (see Supplementary Figure S4B).

Locating *trans-* $2O_{ph}.4O_w$ motifs and their variations: This is probably the most difficult exercise given the ≈4.1 Å distances separating the O_{ph} atoms that overlap with inter-phosphate distances from other motifs (Figures 3 and 7C). However, the use of this distance criterion may accelerate the identification of patterns in *trans-*.

Locating $2O_b$ $.4O_w$ and O_{ph} $.O_b$ $/N_b$ $.4O_w$ motifs: We found only one 'poorly-defined' occurrence of the $2O_b.4O_w$ motif. Therefore, Mg^{2+} is not an ideal ion for bridging O_b atoms from stacked base pairs from consecutive nucleotides in opposition to Na^+/K^+ monovalent ions (15). No $O_{ph}.N_b.4O_w$ and only two 'well-defined' $O_{ph}.4O_w.N_{His}$ motifs were characterized. The slightly more frequent $O_{ph}.O_b.4O_w$ motifs that can also be of the 'intra-nucleotide' type can be located by monitoring $d(O_{ph}...O_b)$ ≤3.4 Å distances.

Locating $2N_b$ $.4O_w$ motifs: Although the stacking distance between two consecutive nucleotides is around ≈3.4 Å, the distance between two stacked purine N7 atoms is often >3.8 Å. Therefore, bidentate binding to a Mg^{2+} ion involving consecutive purines is not observed. In 8b0x, the only nucleobase arrangement where N7 atoms are separated by <3.4 Å are like those shown in Figure 8 and Supplementary Figure S3. Indeed, only three 'head-to-tail purine stacks' were detected. These stacks bind Mg^{2+} or Zn^{2+} ions as suggested elsewhere (16,51). Hence, searches for *cis*-$2N_b.4O_w$-binding patterns involving consecutive purines can be avoided.

Locating $Mg^{2±}$ of the O_{ph} $/O_b$ $/N_b$ $.5O_w$ type: Locating these binding motifs is more difficult but the coordination geometry of the Mg^{2+} ions shown in 6B and may provide some hints (15,16). For $O_{ph}.5O_w$, the Mg^{2+} ion is roughly in the OP-P-OP plane and the P-OP...Mg^{2+} angle is in the 120–160° range. For the $O_b/N_b.5O_w$ variants, the Mg^{2+} ion is in the nucleobase plane. Yet the angle constrains are slightly different with an average (C = O...Mg^{2+}) angle of ≈144°. In this binding mode, the ion is approximately aligned with one of the O_b lone pairs as confirmed by recent simulation data (63). For $N_b.5O_w$ types on the other hand, Mg^{2+} ions are aligned along the N7 lone pair.

Locating $Mg^{2±}$ of the $6O_w$ type: Defining binding rules for the less tightly bound $6O_w$ ions is challenging. Like for $O_{ph}/O_b/N_b.5O_w$, the Mg^{2+} ions of the $6O_w$ type that establish a high number of water-mediated contacts bind strongly to rRNA. Some of these ions are involved in important structural folding 'wedges' (Figure 5A). The fact that these Mg^{2+} ions use their first shell water molecules to bind to appropriate rRNA-binding sites such as the guanine O6/N7 and the OP1/OP2 atoms suggests to scan the rRNA hydration shell to locate potential $6O_w$-binding sites. Indeed, a precise knowledge of the rRNA hydration shell will be helpful to locate the most important water-mediated Mg^{2+}-binding spots. These can be derived from experimental structures and molecular dynamics (MD) simulations for protein and DNA systems (89–93).

Discussion

Stereochemistry is an essential tool for assigning Mg^{2+} ions

Here, we revised the 8b0x structure and completed its solvation shell to obtain insights that could not be derived with the same level of accuracy from lower-resolution structures. We confirmed previously described Mg^{2+}-binding patterns to O_b/N_b atoms (10,15,16,30) and added a comprehensive description of Mg^{2+}-binding patterns to O_{ph} atoms. Our findings, which establish a precise classification of all the Mg^{2+}-binding sites, are summarized in Figure 4.

A key outcome of this study is surprisingly simple and states that Mg^{2+} binding induces unique folding patterns in which rRNA oxygens are separated by ≈2.9 Å (Figure 4). When we applied this criterion, we observed that in every instance where $d(O_{ph}...O_{ph})$ ≤3.4 Å, the two O_{ph} atoms are linked by a Mg^{2+} ion, either through inner-shell contacts or, in two occurrences through a combination of inner- and outer-shell contacts (Supplementary Figure S2). Therefore, we concluded that Mg^{2+} is necessary to stabilize configurations with short inter-O_{ph} distances that correspond to strong electronegative spots in RNA structures. Stabilization of such configurations by Na^+/K^+ ions that display smaller charge densities has not been observed in RNA systems (67).

Although these results need to be confirmed by scanning more RNA structures, we estimate that by using this 2.9 Å distance criterion, we achieved ≈100% accuracy in the identification of *cis*-bidentate Mg^{2+}-binding sites. We also uncovered two novel *cis*-$O_{ph}.O_r$ motifs involving O2' atoms that were, to the best of our knowledge, not documented elsewhere. These Mg^{2+} stabilized motifs involve a specific backbone conformation that places an O2' atom at ≈3.0 Å from an O_{ph} atom of a consecutive nucleotide (Figure 11). Interestingly, this RNA-binding principle also applies to proteins where $d(COO^-...^-OOC)$ <3.4 Å points to *cis*-$2O_{coo}.4O_w$ Mg^{2+} ions, as observed in uS2 (Supplementary Figure S4B). Likewise, a rare $3O_{ph}.O_w.2O_{tetracycline}$ Mg^{2+}-binding mode is seen in antibiotic bound ribosomes (94). However, the application of this criterion might be less effective for lower-resolution structures with less well defined phosphate group positions, resulting in bidentate Mg^{2+}-binding sites with $d(O_{ph}...O_{ph})$ >3.4 Å. Besides locating these clamps, we showed that stereochemical criteria are similarly effective for characterizing $O_{ph}.5O_w$ and $6O_w$ sites that involve a strong correspondence between the Mg^{2+} hydration shell and local nucleotide hydration patterns (Figures 4 and 5).

During the solvent identification process, the density peaks of solvent particles can also provide valuable information. Typically, K^+ ions exhibit higher densities than Mg^{2+} ions and bound water molecules. However this can be misleading since some water molecules involved in strong water-mediated contacts may display higher densities than those associated with the more distant Mg^{2+} ion. In such cases, stereochemistry is of great help for interpreting the binding site structure. Certainly, the interpretation of experimental data must comply with stereochemical rules and any discrepancies should be resolved through additional experiments or adjustments to current paradigms.

Structural ion pairs in ribosomes

The characterisation of ion pairs in 8b0x provides insights into the features of these motifs in both ribosomal and non-ribosomal RNA systems. Since the Steitz proposal of a two-metal-ion catalytic mechanism for RNA splicing and RNase P hydrolysis (95), interest in nucleic acid catalytic sites has grown and has been extended to various RNA systems such as spliceosomes and group I and II introns (77,96–101). K^+ ions involved in ion pairs were also thought to play a role in catalytic systems (102,103).

Besides catalytic mechanisms, the structural role of $Mg^{2+}...Mg^{2+}$ ion pairs has been less thoroughly explored, except for some $MgA_{\mu c}$ pairs observed in several ribosomes (2,6,43,80). In the 8b0x structure, we identified and classified different types of $Mg^{2+}...Mg^{2+}/K^+$ pairs and illustrated how they 'assemble' to form extensive ion chains (Figure 16). This suggests that ion pairs, including those with monovalent

ions (15), frequently occur in RNA systems, although the relationship between their formation and the ionic strength of the buffers is not currently appreciated. In that respect, we note that the +2 net charge on the Mg^{2+} ions forming ion pairs may significantly decrease resulting in a redistribution of the ions electronic charge towards the bound phosphates (60) amplifying polarization and charge transfer effects. This phenomenon has also been discussed for Mg^{2+} ions not involved in ion pairs (2,104).

Hierarchical Mg^{2+} dehydration during ribosome biogenesis

The most intricate ion binding pockets described herein correspond to motifs embedded in the ribosome core during biogenesis. The formation of such motifs requires a level of structural complexity not accessible to smaller RNAs. For instance, Mg^{2+} does not form direct contacts with phosphate oxygens in Watson–Crick helical structures unless non-canonical base pairs are present as in the ribosomal 5S loop E motif (48,79,83). Similarly, few direct Mg^{2+} contacts are observed within transfer RNA (tRNA) structures with resolutions <2.0 Å. An exception is a *cis*-$2O_{ph}.4O_w$ motif observed in the D-loop of a $tRNA^{Phe}$ structure [PDBid: 1EHZ; res. 1.93 Å (105)]. More complex motifs emerge in the ≈400 nucleotide-long Group I introns (106,107). Based on these observations, we suggest that structural complexity is a prerequisite for the formation of higher-order Mg^{2+}-binding modes.

The apparently simple Mg^{2+} binding classification we propose highlights a great diversity of motifs when considering the combinatorial possibilities associated with the relative positions of the coordinating atoms. It also suggests a hierarchical dehydration pathway associated with the formation of these motifs (Figure 17). We infer that the principles described in this study will be particularly useful for groups involved in RNA-folding competitions, such as RNA-puzzle (108,109), as current strategies rarely use information related to water or ion coordination.

Considerations related to buffer and *in vivo* Mg^{2+} concentrations

Biochemical investigations suggested that optimal buffer conditions for ribosomes include 2–5 mM of Mg^{2+} and 60–150 mM of K^+ with 2 mM of spermidine (3,7). Although the 17–20 mM Mg^{2+} concentration in cells is close to the 25 mM present in the 8b0x buffer, the estimated concentration of non-chelated hexahydrated Mg^{2+} ions in a crowded intracellular environment is 1–2 mM (110). The hypothesis of an optimal Mg^{2+} concentration has been examined by several research groups. The addition of weakly chelating agents to buffers has been found to enhance RNA function, chemical stability and catalytic efficiency likely by sequestering divalent ion excess (110–112). Similarly, low Mg^{2+} concentration affect the RNA properties of certain systems by preventing suitable folding while high Mg^{2+} concentrations reduce activity (113). This aligns with findings showing that excess Mg^{2+} reduces ribosomal translational activity and accuracy (7,114). In line with these results, we previously speculated that excess Mg^{2+} may over-stabilize rRNA structures and grip the translation machinery by binding to messenger RNAs and tRNAs, while a less organizing ion such as K^+, may act as a lubricant facilitating a smoother translation process and thereby preserving an optimal turn-over rate (17).

We conjecture that the optimal number of chelated Mg^{2+} ions includes ≈100 *cis*- and *trans*- ions coordinating with at least two non-water oxygen/nitrogen atoms that are for most of them incorporated during ribosome biogenesis. A yet unknown proportion of the ≈290 '$O_{ph}.5O_w/6O_w$' ions which have limited or no access to the bulk solvent may also be captured during biogenesis (Figures 5A and 6A). However, it remains unclear whether all the characterized $O_{ph}.5O_w/6O_w$ ions are essential for ribosome activity or result from an excess of Mg^{2+} ions in cryo-EM buffers. This raises the question of whether the number of Mg^{2+} ions observed in 8b0x exceeds the amounts necessary for a ribosome to perform its *in vivo* tasks (17,88,113).

In summary, reinterpreting the 8b0x structure allowed us to characterize the currently largest number of chelated Mg^{2+}/K^+ ions identified in a ribosome. Yet, the identified Mg^{2+}/K^+ ions that carry a total of ≈1040 positive charges are insufficient to neutralize the ≈5000 rRNA negatively charged nucleotides. This remains true even when considering the ≈525 excess positive charges from all bound r-proteins or the ≈1160 charges from all positively charged Lys/Arg residues. For finding the 'missing' ≈3000 positive charges, theoretical approaches like MD simulations need to be employed (46–48,63,83,115–118).

Amending existing structures

This study also highlights the necessity of revising existing PDB structures, a practice that should be more widely adopted within the structural biology community (19,119). The refinement of the 8b0x structure was clearly not fully completed particularly in terms of the interpretation of its solvation shell. This is understandable given the considerable amount of time required to conduct such a task. PDB structures are a timely interpretation of the experimental data that can be corrected for flaws/omissions as new knowledge becomes available (23,120,121). A good illustration of this process is provided by the multiple corrections made to the *H. marismortui* 50S structure which was first deposited to the PDB in 2000 and last refined in 2013 (9,14). In this study, we significantly improved the 8b0x bacterial ribosomal structure and suggest that a significant number of PDB structures could benefit from similar revisions, particularly regarding their solvation shell and other structurally critical features.

Conclusions

Through a careful analysis of the amended 8b0x bacterial ribosome structure, we examined Mg^{2+}-binding modes and derived a set of ion-binding principles that are based on simple stereochemical rules. These rules will help to develop more accurate solvation shell models for both, small and large RNA structures and led to a comprehensive description of all the major Mg^{2+} chelation sites that involve 2–4 non-water coordinating atoms. These findings will enhance our understanding of RNA folding, structure and catalysis (122). Besides, they will help to improve RNA 3D structure predictions and lead to better designs of structures used to initiate MD simulations (31,89,94,118,123–129).

Data availability

The data underlying this article will be shared on reasonable request to the corresponding author.

Supplementary data

Supplementary Data are available at NAR online.

Acknowledgements

P.A. wishes to thank Dr Yaser Hashem, Dr Quentin Vicens and Prof. Eric Westhof for comments on the manuscript as well as Dr Naleem Nawavi for computational assistance.

Funding

Centre National de la Recherche Scientifique; NYUAD [AD181 to S.K. and A.H.K]; REF [RE317 to S.K. and A.H.K].

Conflict of interest statement

None declared.

References

1. Woodson,S.A. (2011) RNA folding pathways and the self-assembly of ribosomes. *Acc. Chem. Res.*, **44**, 1312–1319.
2. Bowman,J.C., Lenz,T.K., Hud,N.V. and Williams,L.D. (2012) Cations in charge: magnesium ions in RNA folding and catalysis. *Curr. Opin. Struct. Biol.*, **22**, 262–272.
3. Nierhaus,K.H. (2014) Mg^{2+}, K^{+}, and the ribosome. *J. Bacteriol.*, **196**, 3817–3819.
4. Gevrekci,A.O. (2017) The roles of polyamines in microorganisms. *World J. Microbiol. Biotechnol.*, **33**, 204.
5. Trachman,R.J. and Draper,D.E. (2017) Divalent ion competition reveals reorganization of an RNA ion atmosphere upon folding. *Nucleic Acids Res.*, **45**, 4733–4742.
6. Bowman,J.C., A.S.,P. and Williams,L.D. (2018) Role of cations in RNA folding and function. In,Kolb and,V. M. (ed.), *Handbook of Astrobiology*. CRC Press, Boca Raton, pp. 421–435.
7. Akanuma,G. (2021) Diverse relationships between metal ions and the ribosome. *Biosci. Biotechnol. Biochem.*, **85**, 1582–1593.
8. Belinite,M., Khusainov,I., Soufari,H., Marzi,S., Romby,P., Yusupov,M. and Hashem,Y. (2021) Stabilization of ribosomal RNA of the small subunit by spermidine in *Staphylococcus aureus*. *Front. Mol. Biosci.*, **8**, 738752.
9. Ban,N., Nissen,P., Hansen,J., Moore,P.B. and Steitz,T.A. (2000) The complete atomic structure of the large ribosomal subunit at 2.4 Å resolution. *Science*, **289**, 905–920.
10. Klein,D.J., Moore,P.B. and Steitz,T.A. (2004) The contribution of metal ions to the structural stability of the large ribosomal subunit. *RNA*, **10**, 1366–1379.
11. Fromm,S.A., O'Connor,K.M., Purdy,M., Bhatt,P.R., Loughran,G., Atkins,J.F., Jomaa,A. and Mattei,S. (2023) The translating bacterial ribosome at 1.55 A resolution generated by cryo-EM imaging services. *Nat. Commun.*, **14**, 1095.
12. Polikanov,Y.S., Melnikov,S.V., Soll,D. and Steitz,T.A. (2015) Structural insights into the role of rRNA modifications in protein synthesis and ribosome assembly. *Nat. Struct. Mol. Biol.*, **22**, 342–344.
13. Jenner,L.B., Demeshkina,N., Yusupova,G. and Yusupov,M. (2010) Structural aspects of messenger RNA reading frame maintenance by the ribosome. *Nat. Struct. Mol. Biol.*, **17**, 555–560.
14. Gabdulkhakov,A., Nikonov,S. and Garber,M. (2013) Revisiting the *Haloarcula marismortui* 50S ribosomal subunit model. *Acta Crystallogr. D Struct. Biol.*, **69**, 997–1004.
15. Leonarski,F., D'Ascenzo,L. and Auffinger,P. (2019) Nucleobase carbonyl groups are poor Mg^{2+} inner-sphere binders but excellent monovalent ion binders – A critical PDB survey. *RNA*, **25**, 173–192.
16. Leonarski,F., D'Ascenzo,L. and Auffinger,P. (2017) Mg^{2+} ions: do they bind to nucleobase nitrogens? *Nucleic Acids Res.*, **45**, 987–1004.
17. Auffinger,P., Ennifar,E. and D'Ascenzo,L. (2021) Deflating the RNA Mg^{2+} bubble. Stereochemistry to the rescue! *RNA*, **27**, 242–252.
18. Dauter,Z., Wlodawer,A., Minor,W., Jaskolski,M. and Rupp,B. (2014) Avoidable errors in deposited macromolecular structures: an impediment to efficient data mining. *IUCrJ*, **1**, 179–193.
19. Williams,L.D. (2005) Between objectivity and whim: nucleic acid structural biology. *Top. Curr. Chem.*, **253**, 77–88.
20. Minor,W., Dauter,Z., Helliwell,J.R., Jaskolski,M. and Wlodawer,A. (2016) Safeguarding structural data repositories against bad apples. *Structure*, **24**, 216–220.
21. Rupp,B. (2016) Only seeing is believing – the power of evidence and reason. *Postępy Biochemii*, **62**, 250–256.
22. Rupp,B., Wlodawer,A., Minor,W., Helliwell,J.R. and Jaskolski,M. (2016) Correcting the record of structural publications requires joint effort of the community and journal editors. *FEBS J.*, **283**, 4452–4457.
23. Wlodawer,A., Dauter,Z., Porebski,P.J., Minor,W., Stanfield,R., Jaskolski,M., Pozharski,E., Weichenberger,C.X. and Rupp,B. (2018) Detect, correct, retract: how to manage incorrect structural models. *FEBS J.*, **285**, 444–466.
24. Gao,Y., Thorn,V. and Thorn,A. (2023) Errors in structural biology are not the exception. *Acta Crystallogr. D Struct. Biol.*, **79**, 206–211.
25. Zheng,H., Chordia,M.D., Cooper,D.R., Chruszcz,M., Muller,P., Sheldrick,G.M. and Minor,W. (2014) Validation of metal-binding sites in macromolecular structures with the CheckMyMetal web server. *Nat. Protoc.*, **9**, 156–170.
26. Zheng,H., Cooper,D.R., Porebski,P.J., Shabalin,I.G., Handing,K.B. and Minor,W. (2017) CheckMyMetal: a macromolecular metal-binding validation tool. *Acta Crystallogr. D Struct. Biol.*, **73**, 223–233.
27. Gucwa,M., Lenkiewicz,J., Zheng,H., Cymborowski,M., Cooper,D.R., Murzyn,K. and Minor,W. (2023) CMM-an enhanced platform for interactive validation of metal binding sites. *Protein Sci.*, **32**, e4525.
28. Majorek,K.A., Gucwa,M., Murzyn,K. and Minor,W. (2024) Metal ions in biomedically relevant macromolecular structures. *Front. Chem.*, **12**, 1426211.
29. Gucwa,M., Bijak,V., Zheng,H., Murzyn,K. and Minor,W. (2024) CheckMyMetal (CMM): validating metal-binding sites in X-ray and cryo-EM data. *IUCrJ*, **11**, 871–877.
30. Zheng,H., Shabalin,I.G., Handing,K.B., Bujnicki,J.M. and Minor,W. (2015) Magnesium-binding architectures in RNA crystal structures: validation, binding preferences, classification and motif detection. *Nucleic Acids Res.*, **43**, 3789–3801.
31. Marcia,M., Manigrasso,J. and De Vivo,M. (2021) Finding the ion in the RNA-stack: can computational models accurately predict key functional elements in large macromolecular complexes? *J. Chem. Inf. Model.*, **61**, 2511–2515.
32. Zhou,Y. and Chen,S.J. (2022) Graph deep learning locates magnesium ions in RNA. *QRB Discov.*, **3**, e20.
33. Durr,S.L., Levy,A. and Rothlisberger,U. (2023) Metal3D: a general deep learning framework for accurate metal ion location prediction in proteins. *Nat. Commun.*, **14**, 2713.
34. Zheng,H., Zhang,H., Zhong,J., Gucwa,M., Zhang,Y., Ma,H., Deng,L., Mao,L., Minor,W. and Wang,N. (2024) PinMyMetal: a hybrid learning system to accurately model metal binding sites in macromolecules. *Res. Sq.*

35. Wang,K., Yin,Z., Sang,C., Xia,W., Wang,Y., Sun,T. and Xu,X. (2024) Geometric deep learning for the prediction of magnesium-binding sites in RNA structures. *Int. J. Biol. Macromol.*, **262**, 130150.
36. Rozov,A., Khusainov,I., El Omari,K., Duman,R., Mykhaylyk,V., Yusupov,M., Westhof,E., Wagner,A. and Yusupova,G. (2019) Importance of potassium ions for ribosome structure and function revealed by long-wavelength X-ray diffraction. *Nat. Commun.*, **10**, 2519.
37. Watson,Z.L., Ward,F.R., Meheust,R., Ad,O., Schepartz,A., Banfield,J.F. and Cate,J.H. (2020) Structure of the bacterial ribosome at 2 Å resolution. *eLife*, **9**, e60482.
38. Terwilliger,T.C., Sobolev,O.V., Afonine,P.V., Adams,P.D. and Read,R.J. (2020) Density modification of cryo-EM maps. *Acta Crystallogr. D Struct. Biol.*, **76**, 912–925.
39. Yamashita,K., Palmer,C.M., Burnley,T. and Murshudov,G.N. (2021) Cryo-EM single-particle structure refinement and map calculation using Servalcat. *Acta Crystallogr. D Struct. Biol.*, **77**, 1282–1291.
40. Yamashita,K., Wojdyr,M., Long,F., Nicholls,R.A. and Murshudov,G.N. (2023) GEMMI and Servalcat restrain REFMAC5. *Acta Crystallogr. D Struct. Biol.*, **79**, 368–373.
41. Ennifar,E., Walter,P. and Dumas,P. (2003) A crystallographic study of the binding of 13 metal ions to two related RNA duplexes. *Nucleic Acids Res.*, **31**, 2671–2682.
42. El Omari,K., Forsyth,I., Duman,R., Orr,C.M., Mykhaylyk,V., Mancini,E.J. and Wagner,A. (2024) Utilizing anomalous signals for element identification in macromolecular crystallography. *Acta Crystallogr. D Struct. Biol.*, **80**, 713–721.
43. Hsiao,C. and Williams,L.D. (2009) A recurrent magnesium-binding motif provides a framework for the ribosomal peptidyl transferase center. *Nucleic Acids Res.*, **37**, 3134–3142.
44. Bowman,J.C., Petrov,A.S., Frenkel-Pinter,M., Penev,P.I. and Williams,L.D. (2020) Root of the tree: the significance, evolution, and origins of the ribosome. *Chem. Rev.*, **120**, 4848–4878.
45. Fujita,K., Shindo,Y., Katsuta,Y., Goto,M., Hotta,K. and Oka,K. (2023) Intracellular Mg^{2+} protects mitochondria from oxidative stress in human keratinocytes. *Commun. Biol.*, **6**, 868.
46. Auffinger,P. and Westhof,E. (2000) Water and ion binding around RNA and DNA (C,G)-oligomers. *J. Mol. Biol.*, **300**, 1113–1131.
47. Auffinger,P. and Westhof,E. (2001) Water and ion binding around $r(UpA)_{12}$ and $d(TpA)_{12}$ oligomers - comparison with RNA and DNA $(CpG)_{12}$ duplexes. *J. Mol. Biol.*, **305**, 1057–1072.
48. Auffinger,P., Bielecki,L. and Westhof,E. (2004) Symmetric K+ and Mg2+ ion-binding sites in the 5S rRNA loop E inferred from molecular dynamics simulations. *J. Mol. Biol.*, **335**, 555–571.
49. Groom,C.R. and Allen,F.H. (2014) The Cambridge Structural Database in retrospect and prospect. *Angew. Chem. Int. Ed. Engl.*, **53**, 662–671.
50. Taylor,R. and Wood,P.A. (2019) A million crystal structures: the whole is greater than the sum of its parts. *Chem. Rev.*, **119**, 9427–9477.
51. Leonarski,F., D'Ascenzo,L. and Auffinger,P. (2016) Binding of metal ions to purine N7 atoms and implications for nucleic acids: a CSD survey. *Inorg. Chim. Acta*, **452**, 82–89.
52. Shields,G.P., Raithby,P.R., Allen,F.H. and Motherwell,W.D. (2000) The assignment and validation of metal oxidation states in the Cambridge Structural Database. *Acta Crystallogr. B Struct. Biol.*, **56**, 455–465.
53. Auffinger,P., D'Ascenzo,L. and Ennifar,E. (2016) Sodium and potassium interactions with nucleic acids. *Met. Ions Life Sci.*, **16**, 167–201.
54. Li,Z., Song,L.F., Sharma,G., Koca Findik,B. and Merz,K.M. Jr. (2023) Accurate metal-imidazole interactions. *J. Chem. Theory Comput.*, **19**, 619–625.
55. Li,Z., Bhowmik,S., Sagresti,L., Brancato,G., Smith,M., Benson,D.E., Li,P. and Merz,K.M. Jr. (2024) Simulating metal-imidazole complexes. *J. Chem. Theory Comput.*, **20**, 6706–6716.
56. Afonine,P.V., Poon,B.K., Read,R.J., Sobolev,O.V., Terwilliger,T.C., Urzhumtsev,A. and Adams,P.D. (2018) Real-space refinement in PHENIX for cryo-EM and crystallography. *Acta Crystallogr. D Struct. Biol.*, **74**, 531–544.
57. Emsley,P., Lohkamp,B., Scott,W.G. and Cowtan,K. (2010) Features and development of Coot. *Acta Crystallogr. D Struct. Biol.*, **66**, 486–501.
58. Auffinger,P., Bielecki,L. and Westhof,E. (2004) Anion binding to nucleic acids. *Structure*, **12**, 379–388.
59. D'Ascenzo,L. and Auffinger,P. (2016) Anions in nucleic acid crystallography. *Methods Mol. Biol.*, **1320**, 337–351.
60. Glusker,J.P., Katz,A.K. and Bock,C.W. (2001) Two-metal binding motifs in protein crystal structures. *Struct. Chem.*, **12**, 323–341.
61. Puyo-Fourtine,J., Juille,M., Henin,J., Clavaguera,C. and Duboué-Dijon,E. (2022) Consistent picture of phosphate-divalent cation binding from models with implicit and explicit electronic polarization. *J. Phys. Chem. B*, **126**, 4022–4034.
62. Ye,J.D., Tereshko,V., Frederiksen,J.K., Koide,A., Fellouse,F.A., Sidhu,S.S., Koide,S., Kossiakoff,A.A. and Piccirilli,J.A. (2008) Synthetic antibodies for specific recognition and crystallization of structured RNA. *Proc. Natl Acad. Sci. U.S.A.*, **105**, 82–87.
63. Kolev,S.K., St Petkov,P., Milenov,T.I. and Vayssilov,G.N. (2022) Sodium and magnesium ion location at the backbone and at the nucleobase of RNA: ab Initio molecular dynamics in water solution. *ACS Omega*, **7**, 23234–23244.
64. Wang,J., Natchiar,S.K., Moore,P.B. and Klaholz,B.P. (2021) Identification of Mg(2+) ions next to nucleotides in cryo-EM maps using electrostatic potential maps. *Acta Crystallogr. D Struct. Biol.*, **77**, 534–539.
65. Hsiao,C., Tannenbaum,E., VanDeusen,H., Hershkovitz,E., Perng,G., Tannenbaum,A.R. and Williams,L.D. (2009) Complexes of nucleic acids with group I and II cations. In Hud,N. V. (ed.), *Nucleic Acid-Metal Ion Interactions*. Royal Society of Chemistry, Cambridge, pp. 1–38.
66. Lilley,D.M.J. (2019) Classification of the nucleolytic ribozymes based upon catalytic mechanism. *F1000Res*, **8**, F1000 Faculty Rev-1462.
67. Petrov,A.S., Bowman,J.C., Harvey,S.C. and Williams,L.D. (2011) Bidentate RNA-magnesium clamps: on the origin of the special role of magnesium in RNA folding. *RNA*, **17**, 291–297.
68. Bonn-Breach,R., Gu,Y., Jenkins,J., Fasan,R. and Wedekind,J. (2019) Structure of Sonic Hedgehog protein in complex with zinc(II) and magnesium(II) reveals ion-coordination plasticity relevant to peptide drug design. *Acta Crystallogr. D Struct. Biol.*, **75**, 969–979.
69. Langeberg,C.J. and Kieft,J.S. (2023) A generalizable scaffold-based approach for structure determination of RNAs by cryo-EM. *Nucleic Acids Res.*, **51**, e100.
70. Westhof,E., Watson,Z.L., Zirbel,C.L. and Cate,J.H.D. (2023) Anionic G*U pairs in bacterial ribosomal rRNAs. *RNA*, **29**, 1069–1076.
71. Fasnacht,M., Gallo,S., Sharma,P., Himmelstoss,M., Limbach,P.A., Willi,J. and Polacek,N. (2022) Dynamic 23S rRNA modification ho5C2501 benefits *Escherichia coli* under oxidative stress. *Nucleic Acids Res.*, **50**, 473–489.
72. Ihara,T., Ishii,T., Araki,N., Wilson,A.W. and Jyo,A. (2009) Silver ion unusually stabilizes the structure of a parallel-motif DNA triplex. *J. Am. Chem. Soc.*, **131**, 3826–3827.
73. Tanaka,Y., Kondo,J., Sychrovsky,V., Sebera,J., Dairaku,T., Saneyoshi,H., Urata,H., Torigoe,H. and Ono,A. (2015) Structures, physicochemical properties, and applications of T-Hg(II)-T, C-Ag(I)-C, and other metallo-base-pairs. *Chem. Commun.*, **51**, 17343–17360.
74. Auffinger,P. and Ennifar,E. (2017) Nucleic acid nanomaterials: silver-wired DNA. *Nat. Chem.*, **9**, 932–934.
75. Grime,G.W., Zeldin,O.B., Snell,M.E., Lowe,E.D., Hunt,J.F., Montelione,G.T., Tong,L., Snell,E.H. and Garman,E.F. (2020)

High-throughput PIXE as an essential quantitative assay for accurate metalloprotein structural analysis: development and application. *J. Am. Chem. Soc.*, **142**, 185–197.
76. Holvec,S., Barchet,C., Lechner,A., Frechin,L., De Silva,S.N.T., Hazemann,I., Wolff,P., von Loeffelholz,O. and Klaholz,B.P. (2024) The structure of the human 80S ribosome at 1.9 Å resolution reveals the molecular role of chemical modifications and ions in RNA. *Nat. Struct. Mol. Biol.*, **31**, 1251–1264.
77. Yang,W., Lee,J.Y. and Nowotny,M. (2006) Making and breaking nucleic acids: two-Mg^{2+}-ion catalysis and substrate specificity. *Mol. Cell.*, **22**, 5–13.
78. Palermo,G., Cavalli,A., Klein,M.L., Alfonso-Prieto,M., Dal Peraro,M. and De Vivo,M. (2015) Catalytic metal ions and enzymatic processing of DNA and RNA. *Acc. Chem. Res.*, **48**, 220–228.
79. Correll,C.C., Freeborn,B., Moore,P.B. and Steitz,T.A. (1997) Metals, motifs and recognition in the crystal structure of a 5S rRNA domain. *Cell*, **91**, 705–712.
80. Petrov,A.S., Bernier,C.R., Hsiao,C., Okafor,C.D., Tannenbaum,E., Stern,J., Gaucher,E., Schneider,D., Hud,N.V., Harvey,S.C., *et al.* (2012) RNA-magnesium-protein interactions in large ribosomal subunit. *J. Phys. Chem. B*, **116**, 8113–8120.
81. Cate,J.H., Hanna,R.L. and Doudna,J.A. (1997) A magnesium ion core at the heart of a ribozyme domain. *Nat. Struct. Biol.*, **4**, 553–558.
82. Toor,N., Keating,K.S., Taylor,S.D. and Pyle,A.M. (2008) Crystal structure of a self-spliced group II intron. *Science*, **320**, 77–82.
83. Auffinger,P., Bielecki,L. and Westhof,E. (2003) The Mg^{2+} binding sites of the 5S rRNA loop E motif as investigated by molecular dynamics simulations. *Chem. Biol.*, **10**, 551–561.
84. Steinke,F. and Stock,N. (2021) Systematic investigation of new alkaline earth phosphonates based on the linker molecule N,N'-4,4'-bipiperidine-bis(methylenephosphonic acid). *Z. Anorg. Allg. Chem.*, **647**, 1046–1051.
85. Green,S.P., Jones,C. and Stasch,A. (2007) Stable magnesium(I) compounds with Mg–Mg bonds. *Science*, **318**, 1754–1757.
86. Perera,L., Beard,W.A., Pedersen,L.G. and Wilson,S.H. (2017) Hiding in plain sight: the bimetallic magnesium covalent bond in enzyme active sites. *Inorg. Chem.*, **56**, 313–320.
87. Zhao,H., Lin,Z., Lynn,A.Y., Varnado,B., Beutler,J.A., Murelli,R.P., Le Grice,S.F. and Tang,L. (2015) Two distinct modes of metal ion binding in the nuclease active site of a viral DNA-packaging terminase: insight into the two-metal-ion catalytic mechanism. *Nucleic Acids Res.*, **43**, 11003–11016.
88. Yu,T., Jiang,J., Yu,Q., Li,X. and Zeng,F. (2023) Structural insights into the distortion of the ribosomal small subunit at different magnesium concentrations. *Biomolecules*, **13**, 566.
89. Vaiana,A.C., Westhof,E. and Auffinger,P. (2006) A molecular dynamics simulation study of an aminoglycoside/A-site RNA complex: conformational and hydration patterns. *Biochimie*, **88**, 1061–1073.
90. Biedermannova,L., Cerny,J., Maly,M., Nekardova,M. and Schneider,B. (2022) Knowledge-based prediction of DNA hydration using hydrated dinucleotides as building blocks. *Acta Crystallogr. D Struct. Biol.*, **78**, 1032–1045.
91. Cerny,J., Schneider,B. and Biedermannova,L. (2017) WatAA: atlas of protein hydration. Exploring synergies between data mining and ab initio calculations. *Phys. Chem. Chem. Phys.*, **19**, 17094–17102.
92. Biedermannova,L. and Schneider,B. (2016) Hydration of proteins and nucleic acids: advances in experiment and theory. A review. *Biochim. Biophys. Acta*, **1860**, 1821–1835.
93. Biedermannova,L. and Schneider,B. (2015) Structure of the ordered hydration of amino acids in proteins: analysis of crystal structures. *Acta Crystallogr. D Biol. Crystallogr.*, **71**, 2192–2202.
94. Paternoga,H., Crowe-McAuliffe,C., Bock,L.V., Koller,T.O., Morici,M., Beckert,B., Myasnikov,A.G., Grubmuller,H., Novacek,J. and Wilson,D.N. (2023) Structural conservation of antibiotic interaction with ribosomes. *Nat. Struct. Mol. Biol.*, **30**, 1380–1392.
95. Steitz,T.A. and Steitz,J.A. (1993) A general two-metal-ion mechanism for catalytic RNA. *Proc. Natl Acad. Sci. U.S.A.*, **90**, 6498–6502.
96. Jacobsen,D.M., Bao,Z.Q., O'Brien,P., Brooks,C.L. and Young,M.A. (2012) Price to be paid for two-metal catalysis: magnesium ions that accelerate chemistry unavoidably limit product release from a protein kinase. *J. Am. Chem. Soc.*, **134**, 15357–15370.
97. Hwang,W., Yoo,J., Lee,Y., Park,S., Hoang,P.L., Cho,H., Yu,J., Hoa Vo,T.M., Shin,M., Jin,M.S., *et al.* (2018) Dynamic coordination of two-metal-ions orchestrates q-exonuclease catalysis. *Nat. Commun.*, **9**, 4404.
98. Trachman,R.J. 3rd and Ferre-D'Amare,A.R. (2021) An uncommon $[K^{+}(Mg^{2+})_2]$ metal ion triad imparts stability and selectivity to the guanidine-I. *RNA*, **27**, 1257–1264.
99. Luo,B., Zhang,C., Ling,X., Mukherjee,S., Jia,G., Xie,J., Jia,X., Liu,L., Baulin,E.F., Luo,Y., *et al.* (2023) Cryo-EM reveals dynamics of *Tetrahymena* group I intron self-splicing. *Nat. Catal.*, **6**, 298–309.
100. Wilkinson,M.E., Charenton,C. and Nagai,K. (2020) RNA splicing by the spliceosome. *Annu. Rev. Biochem.*, **89**, 359–388.
101. Xu,L., Liu,T., Chung,K. and Pyle,A.M. (2023) Structural insights into intron catalysis and dynamics during splicing. *Nature*, **624**, 682–688.
102. Wilkinson,M.E., Fica,S.M., Galej,W.P. and Nagai,K. (2021) Structural basis for conformational equilibrium of the catalytic spliceosome. *Mol. Cell.*, **81**, 1439–1452 e9.
103. Aupic,J., Borisek,J., Fica,S.M., Galej,W.P. and Magistrato,A. (2023) Monovalent metal ion binding promotes the first transesterification reaction in the spliceosome. *Nat. Commun.*, **14**, 8482.
104. Markham,G.D., Glusker,J.P. and Bock,C.W. (2002) The arrangement of first and second-sphere water molecules in divalent magnesium complexes: results from molecular orbital and density functional theory and from structural crystallography. *J. Phys. Chem. B*, **106**, 5118–5134.
105. Shi,H. and Moore,P.B. (2000) The crystal structure of yeast phenylalanine tRNA at 1.93 Å resolution: a classic structure revisited. *RNA*, **6**, 1091–1105.
106. Juneau,K., Podell,E., Harrington,D.J. and Cech,T.R. (2001) Structural basis of the enhanced stability of a mutant ribozyme domain and a detailed view of RNA-solvent interactions. *Structure*, **9**, 221–231.
107. Su,Z., Zhang,K., Kappel,K., Li,S., Palo,M.Z., Pintilie,G.D., Rangan,R., Luo,B., Wei,Y., Das,R., *et al.* (2021) Cryo-EM structures of full-length *tetrahymena* ribozyme at 3.1 Å resolution. *Nature*, **596**, 603–607.
108. Miao,Z., Adamiak,R.W., Antczak,M., Boniecki,M.J., Bujnicki,J., Chen,S.J., Cheng,C.Y., Cheng,Y., Chou,F.C., Das,R., *et al.* (2020) RNA-puzzles Round IV: 3D structure predictions of four ribozymes and two aptamers. *RNA*, **26**, 982–995.
109. Li,B., Cao,Y., Westhof,E. and Miao,Z. (2020) Advances in RNA 3D structure modeling using experimental data. *Front. Genet.*, **11**, 574485.
110. Yamagami,R., Sieg,J.P. and Bevilacqua,P.C. (2021) Functional roles of chelated magnesium ions in RNA folding and function. *Biochemistry*, **60**, 2374–2386.
111. Yamagami,R., Bingaman,J.L., Frankel,E.A. and Bevilacqua,P.C. (2018) Cellular conditions of weakly chelated magnesium ions strongly promote RNA stability and catalysis. *Nat. Commun.*, **9**, 2149.
112. Yamagami,R., Huang,R. and Bevilacqua,P.C. (2019) Cellular concentrations of nucleotide diphosphate-chelated magnesium ions accelerate catalysis by RNA and DNA enzymes. *Biochemistry*, **58**, 3971–3979.
113. Guth-Metzler,R., Mohamed,A.M., Cowan,E.T., Henning,A., Ito,C., Frenkel-Pinter,M., Wartell,R.M., Glass,J.B. and

Williams,L.D. (2023) Goldilocks and RNA: where Mg^{2+} concentration is just right. *Nucleic Acids Res.*, **51**, 3529–3539.
114. Zhang,J.J., Ieong,K.W., Johansson,M. and Ehrenberg,M. (2015) Accuracy of initial codon selection by aminoacyl-tRNAs on the mRNA-programmed bacterial ribosome. *Proc. Natl Acad. Sci. U.S.A.*, **112**, 9602–9607.
115. Kirmizialtin,S., Pabit,S.A., Meisburger,S.P., Pollack,L. and Elber,R. (2012) RNA and its ionic cloud: solution scattering experiments and atomically detailed simulations. *Biophys. J.*, **102**, 819–828.
116. He,W., Chen,Y.L., Pollack,L. and Kirmizialtin,S. (2021) The structural plasticity of nucleic acid duplexes revealed by WAXS and MD. *Sci. Adv.*, **7**, eabf6106.
117. Sarkar,R., Jaiswar,A., Hennelly,S.P., Onuchic,J.N., Sanbonmatsu,K.Y. and Roy,S. (2021) Chelated magnesium logic gate regulates riboswitch pseudoknot formation. *J. Phys. Chem. B*, **125**, 6479–6490.
118. Byju,S., Hassan,A. and Whitford,P.C. (2023) The energy landscape of the ribosome. *Biopolymers*. **115**, e23570.
119. de Vries,I., Kwakman,T., Lu,X.J., Hekkelman,M.L., Deshpande,M., Velankar,S., Perrakis,A. and Joosten,R.P. (2021) New restraints and validation approaches for nucleic acid structures in PDB-REDO. *Acta Crystallogr. D Struct. Biol.*, **77**, 1127–1141.
120. Liebschner,D., Afonine,P.V., Moriarty,N.W., Poon,B.K., Chen,V.B. and Adams,P.D. (2021) CERES: a cryo-EM re-refinement system for continuous improvement of deposited models. *Acta Crystallogr. D Struct. Biol.*, **77**, 48–61.
121. Moore,P.B. (2021) The PDB and the ribosome. *J. Biol. Chem.*, **296**, 100561.
122. Vicens,Q. and Kieft,J.S. (2022) Thoughts on how to think (and talk) about RNA structure. *Proc. Natl Acad. Sci. U.S.A.*, **119**, e2112677119.
123. Auffinger,P. (2006) Molecular dynamics simulations of RNA systems: importance of the initial conditions. In Sponer,J. and Lankas,F. (eds.), *Computational Studies of DNA and RNA.*, Springer Verlag, Vol. **II**, pp. 283–300.
124. Jung,J., Nishima,W., Daniels,M., Bascom,G., Kobayashi,C., Adedoyin,A., Wall,M., Lappala,A., Phillips,D., Fischer,W., *et al.* (2019) Scaling molecular dynamics beyond 100,000 processor cores for large-scale biophysical simulations. *J. Comput. Chem.*, **40**, 1919–1930.
125. Sanbonmatsu,K.Y. (2019) Large-scale simulations of nucleoprotein complexes: ribosomes, nucleosomes, chromatin, chromosomes and CRISPR. *Curr. Opin. Struct. Biol.*, **55**, 104–113.
126. Ahn,M., Wlodarski,T., Mitropoulou,A., Chan,S.H.S., Sidhu,H., Plessa,E., Becker,T.A., Budisa,N., Waudby,C.A., Beckmann,R., *et al.* (2022) Modulating co-translational protein folding by rational design and ribosome engineering. *Nat. Commun.*, **13**, 4243.
127. Watson,Z.L., Knudson,I.J., Ward,F.R., Miller,S.J., Cate,J.H.D., Schepartz,A. and Abramyan,A.M. (2023) Atomistic simulations of the *Escherichia coli* ribosome provide selection criteria for translationally active substrates. *Nat. Chem.*, **15**, 913–921.
128. Wych,D.C., Aoto,P.C., Vu,L., Wolff,A.M., Mobley,D.L., Fraser,J.S., Taylor,S.S. and Wall,M.E. (2023) Molecular-dynamics simulation methods for macromolecular crystallography. *Acta Crystallogr. D Struct. Biol.*, **79**, 50–65.
129. Mukherjee,S., Moafinejad,S.N., Badepally,N.G., Merdas,K. and Bujnicki,J.M. (2024) Advances in the field of RNA 3D structure prediction and modeling, with purely theoretical approaches, and with the use of experimental data, *Structure*, **S0969-2126**, 332-0.
130. Hennings,E., Schmidt,H. and Voigt,W. (2013) Crystal structures of hydrates of simple inorganic salts. I. Water-rich magnesium halide hydrates $MgCl_2.8H_2O$, $MgCl_2.12H_2O$, $MgBr_2.6H_2O$, $MgBr_2.9H_2O$, $MgI_2.8H_2O$ and $MgI_2.9H_2O$. *Acta Crystallogr. C Struct. Biol.*, **C69**, 1292–1300.
131. Gerasimchuk,N.N. and Dalley,N.K. (2004) Demetallation of a Ni(II) tetraazamacrocyclic complex by cyanoxime resulting in the formation of a stereospecific trinuclear compound $[Na(H_2O)_6]^+[NaNi_2L_6]^-$ (L = NC-C(NO)-C(O)NH_2^-). *J. Coord. Chem.*, **57**, 1431–1445.
132. Noeske,J., Wasserman,M.R., Terry,D.S., Altman,R.B., Blanchard,S.C. and Cate,J.H. (2015) High-resolution structure of the *Escherichia coli* ribosome. *Nat. Struct. Mol. Biol.*, **22**, 336–341.

Received: April 9, 2024. **Revised:** July 22, 2024. **Editorial Decision:** September 8, 2024. **Accepted:** November 1, 2024